

Shape-dependent settling velocity of skeletal carbonate grains: Implications for calciturbidites

ARNOUD SLOOTMAN^{*,1} , MAX DE KRUIJF[†] , GUENTHER GLATZ^{*} ,
JORIS T. EGGENHUISEN[‡] , RAINER ZÜHLKE[§]  and JOHN J. G. REIJMER^{*,¶,***} 

^{*}College of Petroleum Engineering and Geosciences, King Fahd University of Petroleum & Minerals, Dhahran 31261, Saudi Arabia (E-mail: slootman@mines.com)

[†]IF Technology, Velperweg 37, Arnhem 6824 BE, The Netherlands

[‡]Department of Earth Sciences, Utrecht University, Utrecht, The Netherlands

[§]Geology Technology Team, EXPEC Advanced Research Center, Saudi Aramco, Dhahran, Saudi Arabia

[¶]Department of Earth Sciences, Faculty of Science, Vrije Universiteit Amsterdam, De Boelelaan 1085, Amsterdam 1081 HV, The Netherlands

^{***}Department of Geosciences – Geology, University of Fribourg, Chemin du Musée 6, Fribourg CH-1700, Switzerland

Associate Editor – Fabrizio Felletti

ABSTRACT

Particle transport and deposition in turbidity currents is governed by the balance between turbulent suspension and gravitational settling, with settling velocity becoming dominant during the final rain-out phases of decelerated turbidity currents on lobes. Differential particle settling velocities play a role in the sorting of grains in turbidity currents; there is a preference of grains with higher settling velocities to be deposited first, yielding a settling-velocity gradient in vertical and longitudinal cross-sections through turbidite beds. If sediments contain little variation in particle shape and density (for example, siliciclastics), then settling velocity is dominantly controlled by grain size. Carbonate sediments, in contrast, are composed of non-skeletal and skeletal grains with various growth structures, producing a wide distribution of particle shapes (from spheroidal to platy, bladed and elongated forms). The present paper aims to constrain the extent to which shape-dependent differential settling velocities influence sorting mechanisms in carbonate turbidity currents. Experiments using natural skeletal sand were conducted to investigate the settling of carbonate grains in: (i) isolation; (ii) suspension clouds; and (iii) turbidity currents. Size, density and shape parameters, including Corey Shape Factor and Zingg diagrams, were analysed using high-resolution micro-computed tomography. The slower settling of non-spheroidal shapes was quantified. In the sinking suspensions, a sorting mechanism operated through differential velocities yielding an abundance of spheroidal grains at the base and enrichment in less-spheroidal grains towards the top of suspension deposits. This trend was also observed longitudinally in carbonate turbidity currents, for which enhanced advection lengths caused less spheroidal grains to be transported farther into the basin. The effect of particle shape becomes increasingly significant as grain size increases, in particular above medium sand. Carbonate turbidites may therefore be more poorly sorted than

¹Present address: Department of Geology and Geological Engineering, Colorado School of Mines, Golden, CO, USA

siliciclastic turbidites, which is expected to result in lower primary porosity in calciturbidites compared to siliciclastic turbidites.

Keywords Calciturbidites, calciturbidites, carbonate grains, experiments, micro-CT, particle shape, settling velocity.

INTRODUCTION

Carbonate turbidity currents are subaqueous density flows of suspended sediment particles of CaCO_3 composition. Suspensions of carbonate grains are formed when skeletal remains and non-skeletal particles such as ooids and pellets, together with carbonate mud, are shed off carbonate platforms, for example, during storms and subaqueous slope failures (e.g. Haak & Schlager, 1989; Reijmer *et al.*, 1992, 2012, 2015; Wilson & Roberts, 1992, 1995; Spence & Tucker, 1997; Hickey *et al.*, 2000; Counts *et al.*, 2021; Le Goff *et al.*, 2021). Such suspended sediments may transform into bottom-hugging flows, known as turbidity currents (Kuenen, 1937). The deposits of carbonate turbidity currents are called calciturbidites (Meischner, 1964) and make up significant portions of slope and basinal successions surrounding modern and ancient carbonate platforms (modern examples: Austin Jr. *et al.*, 1986; Eberli *et al.*, 1997; Swart *et al.*, 2000; Shipboard Scientific Party, 2001; Betzler *et al.*, 2017; review of ancient examples: Payros & Pujalte, 2008).

Particles in turbidity currents are kept in suspension for as long as grain-support mechanisms (in particular turbulent mixing) create an upward particle flux that equals or exceeds the downward particle settling flux (Felix, 2002). In proximal slope environments, upward particle flux can be larger than the downward settling flux due to entrainment of seafloor sediments and turbulent mixing, leading to bypass (Stevenson *et al.*, 2015), auto-suspension (Pantin, 1979; Sequeiros *et al.*, 2009) or even flow ignition (Fukushima *et al.*, 1985; Parker *et al.*, 1986; Heerema *et al.*, 2020). The role of particle settling becomes progressively more important as turbidity currents decelerate from the base of slope onward, leading to deposition of settling suspended sediments in submarine lobes (Normark, 1970; Posamentier & Kolla, 2003). Continued deceleration further abates fluid turbulence and all grains eventually deposit. Particle settling from the advecting turbidity current thus becomes the dominant process in distal parts of turbidity current systems.

Particle settling velocity depends on the balance between submerged particle weight and friction

with the water. The size, shape and density of grains, therefore, ultimately control their settling velocity (e.g. Komar & Reimers, 1978; Dietrich, 1982; Ferguson & Church, 2004). Internal porosity may significantly lower the density of the particle, especially for skeletal remains of carbonate-secreting organisms (e.g. Plumley *et al.*, 1962; Folk & Robles, 1964; Swinchatt, 1965; Pilkey *et al.*, 1967; Yordanova & Hohenegger, 2007; Caromel *et al.*, 2014). Form, roundness and surface texture are the three hierarchical parameters of shape (Griffiths, 1967; Barrett, 1980), with *form* being the most important, capturing the particle's dimensions and proportions. The growth habit of carbonate-secreting organisms is such that their skeletal remains adopt a much broader range of forms compared to siliciclastic sediment (Maiklem, 1968; Braithwaite, 1973; Kench & McLean, 1996). Therefore, particle form is a key parameter for the prediction of the settling velocity of biogenic carbonate grains.

The horizontal transport distance of a particle before its final deposition (i.e. advection length) can be estimated from the horizontal velocity of the flow and particle settling time, which depends on the height of the particle above the bed and its settling velocity (Mulder & Alexander, 2001; Lamb *et al.*, 2010; Ganti *et al.*, 2014). Experiments demonstrated that advection length is capable of predicting a first-order scale of submarine lobe dimensions (Spychala *et al.*, 2020). Because particles in turbidity currents attain differential settling velocities, grains reach the bed at different positions along the turbidity current's path (Bornhold & Pilkey, 1971; Stammer, 2014). As a consequence of this longitudinal sorting mechanism, proximal turbidites are enriched in grains with higher settling velocities and grade distally into deposits dominated by particles with lower settling velocities (Pyles *et al.*, 2013; Counts *et al.*, 2021; Le Goff *et al.*, 2021). This trend is also evident in vertical cross-sections of deposits, because at a fixed point on the bed faster-settling grains reach the bed before slower ones (Fig. 1).

These concepts have been extensively explored for siliciclastic turbidites (e.g. van Tassell, 1981; Kneller & McCaffrey, 2003; Talling *et al.*, 2007; Pyles *et al.*, 2013), but have received little

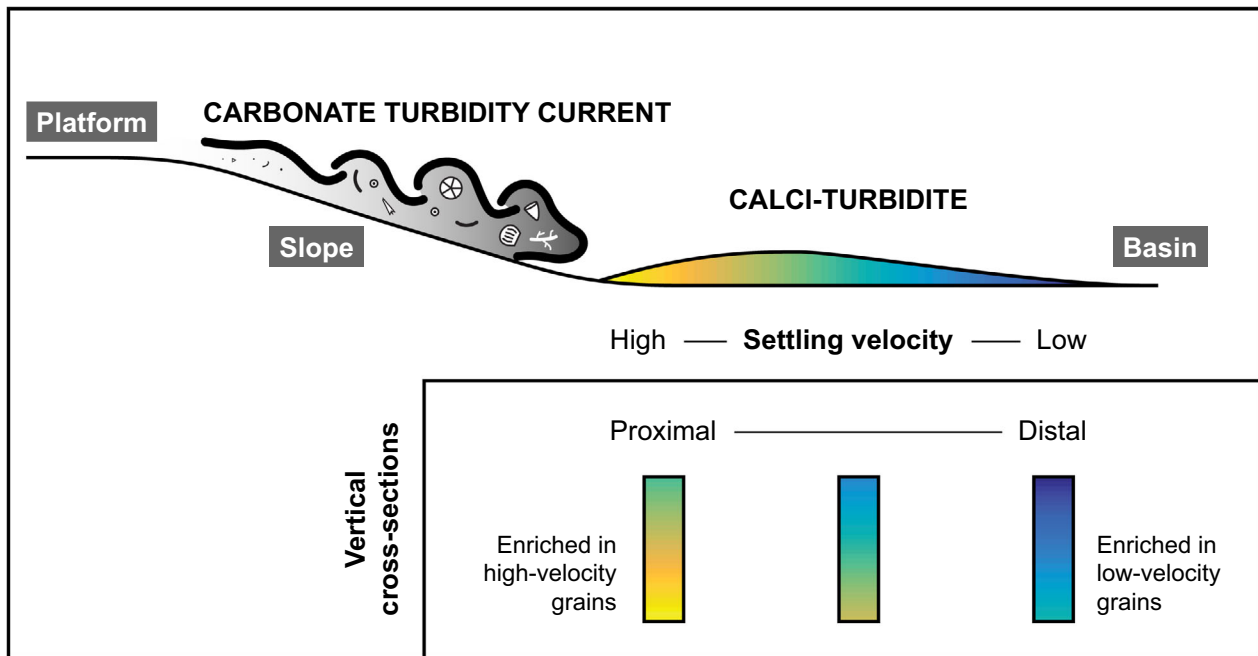


Fig. 1. Deposition of calciturbidites from carbonate turbidity currents. Carbonate grains with higher settling velocity are preferentially deposited in the proximal lobe, while particles with lower settling velocity reach more distal locations. This trend is also reflected in vertical sections across a calciturbidite bed (inset).

attention for turbidites of carbonate composition (Hodson & Alexander, 2010). In turbidity currents transporting quartz grains, the highest settling velocities are reached by coarser particles, while finer grains with lower settling velocities remain in suspension for longer; forming a fining-upward succession when they eventually are deposited (Kuenen & Migliorini, 1950). Carbonate sediments potentially have a wider distribution of particle shape and density, such that settling velocity depends not solely on particle size. Thus, while hydraulic sorting on the basis of settling velocity depends entirely on grain-size distribution for spherical sediments, this is not true for irregular sediments for which shape sorting disturbs trends of distal-fining and upward-fining. The hydrodynamics associated with the irregular nature of skeletal carbonates should therefore be incorporated into calciturbidite models. The present contribution investigates depositional fractionation due to differential settling velocities caused by variations in particle shape within suspensions of carbonate sand.

Knowledge on hydrodynamic sorting mechanisms of particles, and their spatial distribution in associated deposits, has a wide range of applications. From an economic perspective, resedimented carbonates in the subsurface, including

calciturbidites, host large proven hydrocarbon reservoirs (for example, Poza Rica, Mexico: Enos, 1977; Loucks *et al.*, 2011; Janson *et al.*, 2011; Makassar Straits, Indonesia: Pireno *et al.*, 2009; Tanos *et al.*, 2012; North Caspian Basin, Kazakhstan: Cook *et al.*, 2003, 2007; Delaware Basin, New Mexico: Kvale *et al.*, 2020; Presalt Campos Basin, Brazil: Goldberg *et al.*, 2017), and potential new and underexplored ventures (for example, Ionian Sea, Greece: Karakitsios, 2013; South Adriatic Sea, Croatia: Mazzuca *et al.*, 2015; South China Sea: Gong *et al.*, 2014; Lu *et al.*, 2018). Currently, calciturbidites are also being explored for geothermal exploitation (for example, in The Netherlands: Reijmer *et al.*, 2017; Mozafari *et al.*, 2019; Mijndelief, 2020). Carbonate models involving differential shape-dependent settling velocities may be used to predict which components are likely to be exported from the platform environment towards the basin (Braithwaite, 1973; Counts *et al.*, 2021; Le Goff *et al.*, 2021) and are therefore invaluable for source-to-sink studies in carbonate systems (Morgan & Kench, 2016; Jorjy *et al.*, 2020). Applications are also found in marine engineering projects in carbonate environments, including beach erosion, coastal construction, dredging and replenishment works (Murff, 1987; Hohenegger, 2006; Ngan-Tillard *et al.*, 2009; Gailani *et al.*, 2016;

Lokier & Fiorini, 2016; Mohr *et al.*, 2016; Shen *et al.*, 2019). Also, the reconstruction of palaeohydrodynamic conditions and processes in the geological record benefits from an improved understanding of hydrodynamic sorting mechanisms of carbonate sediments (Van Tassell, 1981; Bábek & Kalvoda, 2001; Maurer *et al.*, 2003).

The aim of the present paper is to determine whether differential shape-dependent settling velocities of carbonate grains yield a sorting mechanism for suspension fallout deposits, in particular calciturbidites. Three types of experiments were conducted using natural sand-size carbonate grains with an inherently broad distribution of particle forms: (i) single-grain (SG) settling to establish shape-dependent velocity differences; (ii) suspension-cloud (SC) settling to quantify vertical sorting trends; and (iii) turbidity-current experiments to examine longitudinal sorting trends. This paper is novel in its approach to understanding fractionation in carbonate-sand suspensions using natural skeletal sediment. Differences in sorting and primary porosity distribution between siliciclastic and carbonate turbidites are explored. It is shown that classic (siliciclastic) turbidite models are not sufficient to capture all relevant variations in carbonate turbidites.

METHODS AND MATERIALS

Sediment used in the experiments

Sediment selection

The experiments were carried out using natural carbonate grains eroded from Pleistocene cliffs on Favignana Island, Italy. The sediment is an assemblage of *heterozoan* skeletal remains (James, 1997), which is associated with a cool-water carbonate factory (Schlager, 2000, 2003; Reijmer, 2021). Skeletal components comprise the remains of red algae, molluscs, bryozoans, benthic foraminifera, echinoids, serpulids and barnacles (Sloomman *et al.*, 2019). Each of the three series of experiments (single grains, suspension clouds and turbidity currents) was conducted using a finer-grained and a coarser-grained sediment population to investigate the effects of grain size. The six sediment populations used in the experiments were created from the bulk-collected sediment by careful wet sieving using a series of stacked sieves with half-phi intervals to produce narrow grain-size bins (upper and lower bins of Wentworth, 1922). Sediment was sieved in batches of

100 to 200 g for a duration of 5 to 10 min. The workflow is summarized in Fig. 2.

Micro-computed tomography scanning

The detailed three-dimensional spatial distribution of each particle was measured with micro-computed tomography (micro-CT) at a resolution of *ca* 10 μm , which enabled the accurate reconstruction of particle form. The sand-grade grains collected from experiment samples and bulk sediment populations were fixed into epoxy resin (density 1.07 mg/mm^3) in a cylindrical cup. Particles that were touching one another were discarded, in particular to prevent misidentification of particle aggregates. For single-grain experiments the position of particles within the cup was registered to enable cross-referencing individual grains to their associated experiment run. In addition, the mass of these particles was determined on a balance with a precision of 10 μm to check for unwanted correlations between particle mass and particle form, as well as for calibration of micro-CT-measured particle volume (see below). For the suspension-cloud and turbidity-current experiments, the hundreds of particles collected from each sample were grouped into designated layers in the epoxy resin cup, yet measurement and digital modelling took place for each individual particle (Table 1). Digital grain models were acquired using the FEI Heliscan microCT (Thermo Fisher Scientific, Waltham, MA, USA) at the Center for Integrative Petroleum Research at King Fahd University (Dhahran, Saudi Arabia), configured to perform 1800 projections per revolution at a tube voltage of 85 kV and a current of 72 mA with an exposure time of 1 s. This method captured a series of two-dimensional planar X-ray images used to reconstruct the data into two-dimensional cross-sectional slices that were further processed into three-dimensional models consisting of a collection of voxels (three-dimensional pixels) with dimensions of *ca* $10 \times 10 \times 10 \mu\text{m}^3$ (Fig. 3). The estimated measurement error is *ca* 15 μm in all directions. Dust particles in sample cups constituted a very distinctive size population (>10 times smaller than the sieve size) and were digitally filtered out by applying a grain-size threshold. A cup could hold a maximum of six grain layers. In total 5335 particles were scanned (Table 1).

Grain models consist of 10^4 to 10^6 voxels (step b1 in Table 2). Each voxel is attributed an intensity property (step b2), as a function of absorption/attenuation of the X-ray beam, that is linearly proportional to the mass within that voxel. Because

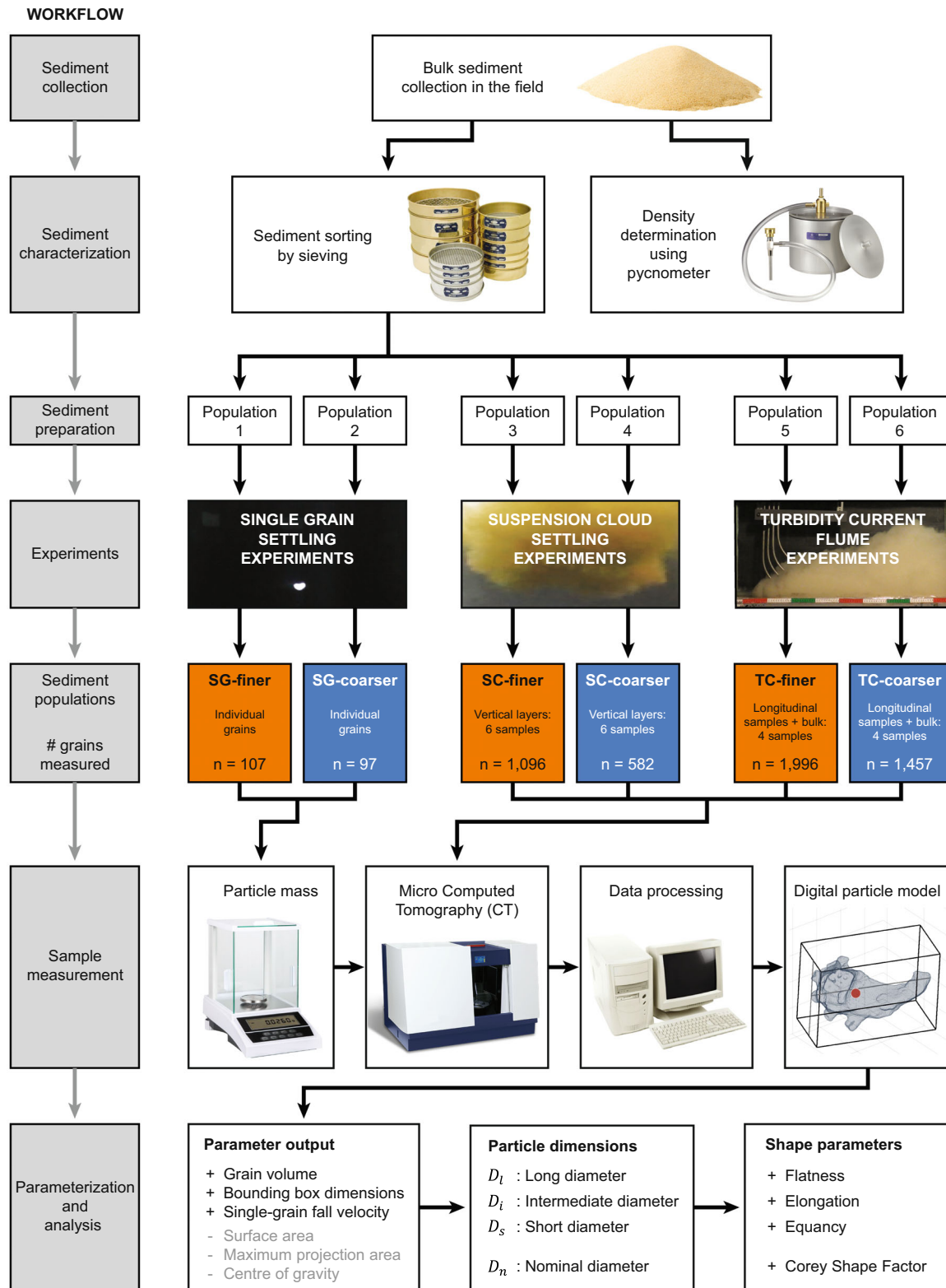


Fig. 2. Workflow chart. Collected sediment was split into six sediment populations to be used in three sets of experiments, each with a finer and coarser grain-size distribution. Digital particle models were created using micro-computed tomography (micro-CT). Particle dimensions and shape parameters were obtained from the digital models.

Table 1. Sediment analysed using micro-computed tomography.

Experiment series	Sediment population	Number of experiments	Analysed sediment	Number of grains measured
Single grains	SG-finer	107	107 individual grains	107
	SG-coarser	97	97 individual grains	97
Suspension clouds	SC-finer	1	Deposit was split into 20 layers. Measured layers: 1 (base), 4, 8, 12, 16, 20 (top)	138 + 154 + 181 + 182 + 246 + 195 = 1096
	SC-coarser	1	Deposit was split into 10 layers. Measured layers: 1 (base), 2, 4, 6, 8, 10 (top)	78 + 106 + 91 + 105 + 101 + 101 = 582
Turbidity currents	TC-finer	1	Bulk sediment used to create turbidity current.	365 + 495 + 678 + 458 = 1996
	TC-coarser	1	Three samples of the turbidite: proximal, intermediate and distal	326 + 363 + 280 + 488 = 1457

some voxels may only be partially filled with solid volume, for example, as a result of crystal-scale microporosity or due to the location of that voxel at the outer limits of the grain, intensity values differ between voxels. The number of voxels, therefore, does not represent the real particle volume. A calibration had to be performed to correct for the mismatch between the reconstructed particle volume (step d1) and the real particle volume used for further analysis (step d2). First, bulk calculations were made for the two cups separately, because they were measured in two runs with different settings. The real volume of all grains together in a cup was determined from the sum of particle masses over the bulk density (step c1). In the model, particle mass is expressed in intensity units (step b2). A volumetric intensity property (step c2), which indicates the number of intensity units per mm^3 , can then be used to find the real volume of an individual particle using the number of intensity units for that specific particle (step d2). The results show that the real volume is about 84% of the volume reconstructed in the CT model (step d3 in Table 2). With these data also the mineral density of individual particles was calculated (see Table S1).

Sediment properties

Particle shape-distribution and size-distribution analysis. Particle shape is commonly parameterized with a long (D_l), intermediate (D_i) and short diameter (D_s) of an ellipsoid in a tri-axial orthogonal system, with D_l chosen along the longest possible diameter. A bounding box with axes parallel to those of the ellipsoid (Krumbein, 1941) suits as a visualization method of

particle dimensions (Fig. 4A). Values for D_s , D_i and D_l were derived from the digital particle models obtained using micro-CT. Ratios of the principal axes, with values from zero to one, are used to compute *flatness* (D_s/D_i), *elongation* (D_i/D_l) and *equancy* (D_s/D_l) (Fig. 4B), only two of which are required to define particle form. An equancy index of one indicates maximum equancy. A value of one for flatness or elongation indices indicates minimum flatness and elongation.

A useful tool for the comparison of particle forms is the Zingg (1935) diagram, which plots flatness against elongation. The diagram is classically divided into four fields (at a value of 2/3 for both indices), discriminating four principal forms: *equant* particles or *spheroids* (neither flat nor elongated), *plates* or *discs* (flat but not elongated), *rods* (elongated but not flat) and *blades* (both flat and elongated; Fig. 5). The Zingg diagram was further subdivided into 9×9 equal squares to allow for a better visualization than the four discrete classes in the original diagram (Fig. 6). The corresponding squares of the Zingg diagram were colour-coded using a temperature scale according to the percentage of grains falling into each of the smaller squares. Using matrix calculations, the difference in form distribution between samples was obtained, which is displayed in a 'difference plot' (Fig. 6). A negative difference (red shade) indicates that in the first diagram (Sample 1) a higher percentage of grains plotted in that square than in the same square in the second diagram (Sample 2). A positive difference (green shade) indicates the opposite. In other words, red areas imply depletion and green areas signify enrichment in those forms, with brightness indicating the intensity of

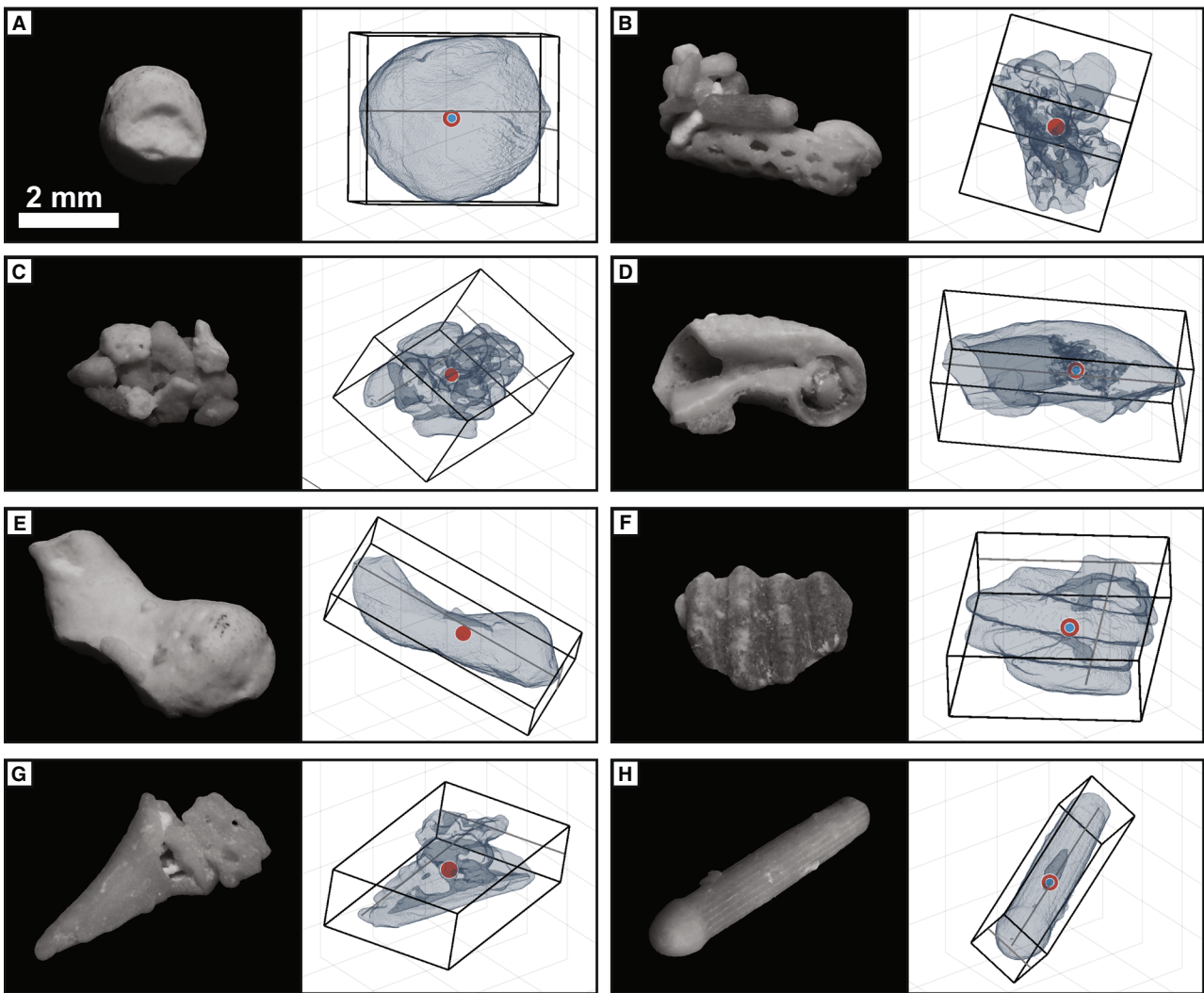


Fig. 3. Black and white reflected-light photographs (left) and digital models (right) of selected carbonate particles used for the single-grain settling experiments. Photographs are all at the same scale; digital models are scaled to fit the frame. Bounding boxes of Krumbein (1941) circumscribe the models. Form classification of these grains is shown in the Zingg diagram in Fig. 5. Particle composition: (A) red algae; (B) aggregate clast with bryozoa fragment; (C) aggregate clast; (D) central coil fragment of gastropod; (E) red algae; (F) bivalve; (G) top coil fragment of gastropod; and (H) echinoid spine.

the difference. Black squares correspond to no difference in that particle form between the two samples.

A practical parametrization of particle form is the Corey (1949) Shape Factor, computed as the square root of the product of flatness and equancy ($CSF = \frac{D_s}{\sqrt{D_l D_t}}$). The Corey Shape Factor (CSF) measures the degree of ellipsoidity and decreases as particles become less spherical, such that lower CSF values may pertain to multiple classes in the Zingg diagram (Fig. 5). The nominal diameter of Wadell (1932) represents a measure of particle

volume ($D_n = \sqrt[3]{6V/\pi}$). The nominal diameter is often obtained from the long, intermediate and short diameters ($D_n = \sqrt[3]{D_l D_t D_s}$), however this method overestimates the characteristic grain size with *ca* 30% in the present dataset (Slootman *et al.*, 2023). The nominal diameter is used here for the analysis of grain-size distribution. Particle-shape and grain-size distributions are expressed as normal-gamma Probability Density Functions (PDFs; Vaz & Fortes, 1988) calculated based on a histogram, which is not always displayed for visualization considerations. Normal-gamma PDFs

Table 2. Workflow for calibration of particle models.

Step	Quantification				Object			
	Symbol	Physical quantity	Method	Unit	Voxel	Particle	Cup 1	Cup 2
(a) Particle selection								
	n	Number of particles	Counting	Count		1	100	104
	m	Mass	Balance	mg		0.47 to 18.61	878.72	129.30
	ρ_{bulk}	Bulk density	Pycnometer	mg/mm ³			2.6939	2.6939
(b) Micro-CT analysis								
	R	Scan resolution	Micro-CT	mm ³ /voxel			1.24658×10^{-8}	1.15903×10^{-8}
b1	V_{model}	Model volume	Micro-CT	Voxels	1	10^4 to 10^6	1.98×10^8	3.65×10^7
b2	I	Intensity property	Micro-CT	Intensity units	130 (average)	10^7 to 10^8	2.29×10^{10}	5.32×10^9
(c) Calculations for bulk								
c1	$V_{\text{real-bulk}}$	Real volume	$\frac{m}{\rho_{\text{bulk}}}$	mm ³		Cannot be calculated directly*	326.19	47.997
c2	ψ	Volumetric intensity property	$\frac{I}{V_{\text{real}}}$	Intensity units/mm ³			7.03×10^7	1.11×10^8
(d) Calculations for individual particle								
d1	$V_{\text{reconstr.}}$	Reconstructed volume using scan resolution	$R \times V_{\text{model}}$	mm ³		Reconstructed particle volume		
d2	$V_{\text{real-part.}}$	Real volume calculated using intensity property	$\frac{I_{\text{particle}}}{\psi_{\text{cup}}}$	mm ³		Real particle volume		
d3	X	Correction factor	$\frac{V_{\text{real}}}{V_{\text{reconstruct}}}$	(–)		0.780 to 0.888	0.847 (average)	0.841 (average)

*Density differs between particles. Individual particle density is not measured, but is eventually determined using particle mass and reconstructed particle volume (step d1).

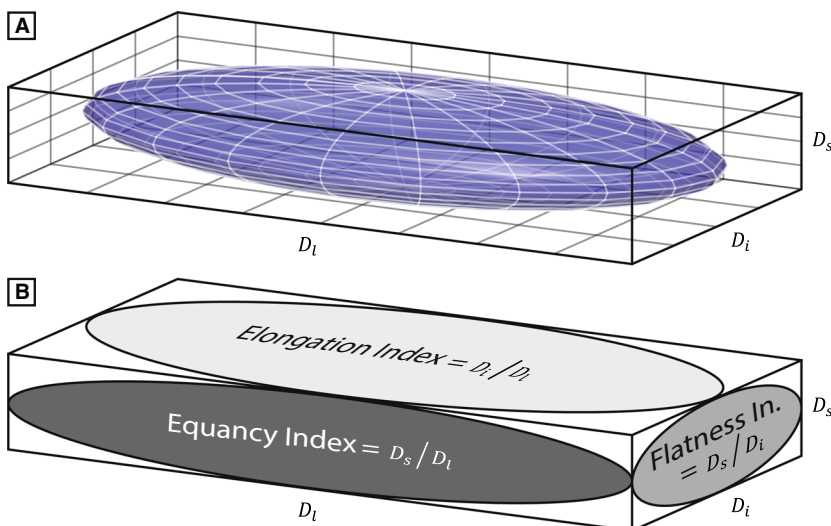


Fig. 4. Particle form is approximated by an ellipsoid with the dimensions of the perpendicular axes of the particle. The bounding box of Krumbein (1941) has the same axes as the ellipsoid. Three axial dimensions define particle flatness, elongation and equancy. These are the projection areas of the ellipsoid onto the bounding box.

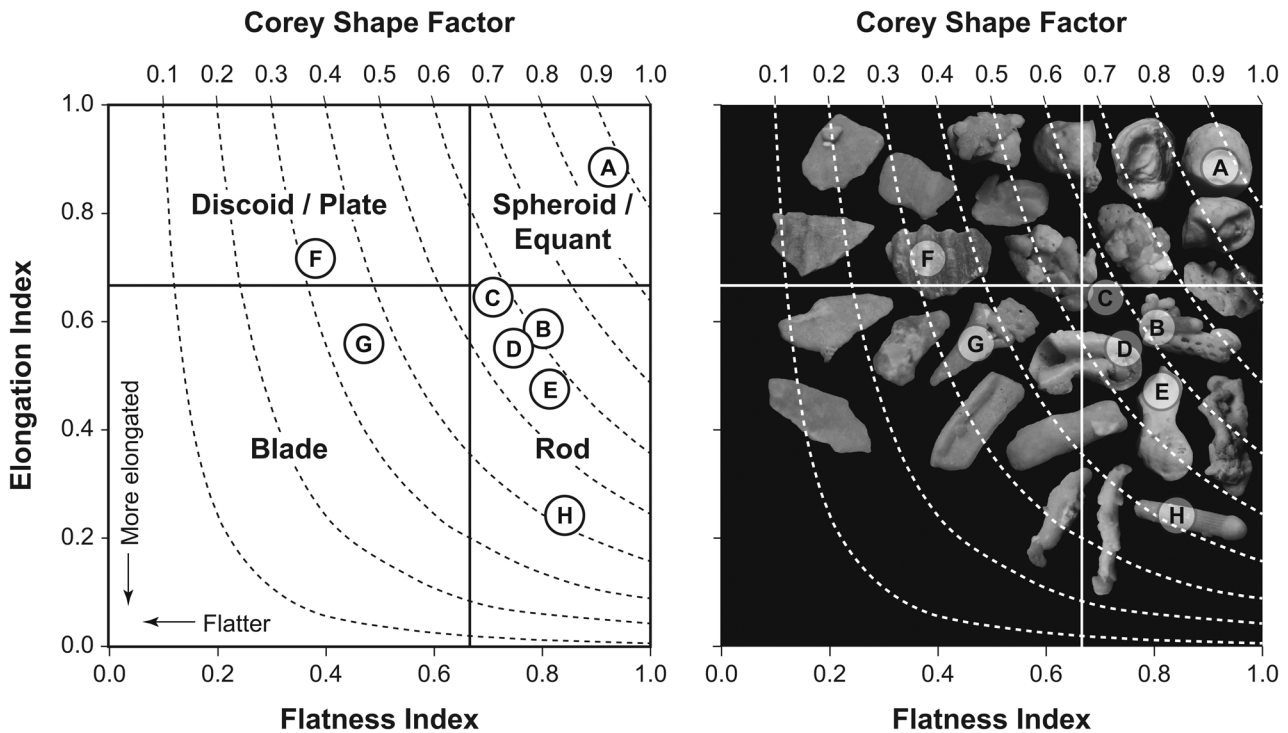


Fig. 5. Form classification in the Zingg (1935) diagram based on flatness and elongation. Particles are least flat and least elongated when their indices equal one (perfect sphere). Dashed isolines of the Corey (1949) Shape Factor are shown. Encircled letters on particle photographs indicate the form class of the selected grains in Fig. 3.

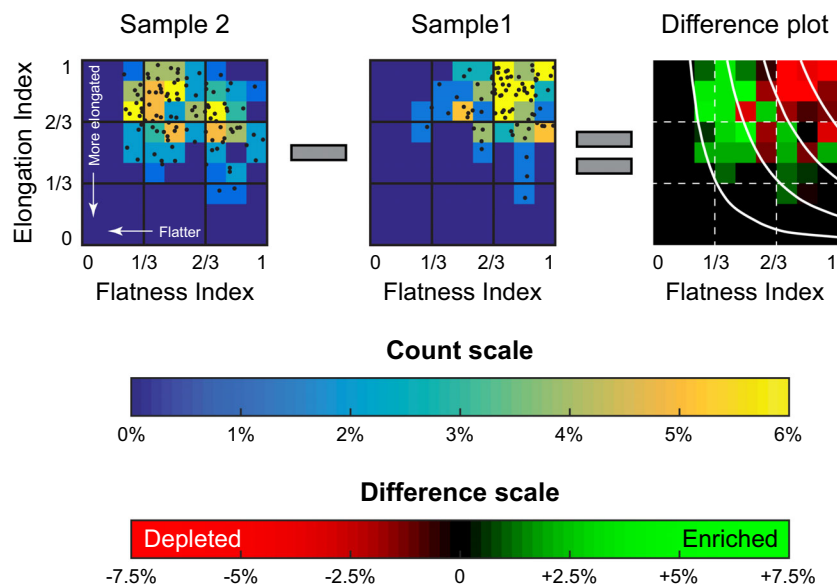


Fig. 6. Representation of form distribution in two samples and the difference between them. The Zingg diagram is further subdivided into 9×9 squares. The percentage of grains (black dots) falling into each of the squares is computed and colour-coded. The difference in counts between Sample 2 and Sample 1 for each small square is calculated and shown in the difference plot. (For each square: Difference = Count Sample 2 – Count Sample 1.) Red shades imply depletion of those particle forms in Sample 2 with respect to Sample 1; green shades signify enrichment. Brightness indicates the intensity of the difference. Corey Shape Factor (CSF) isolines are shown on the difference plot, demonstrating the shift in shape relative to CSF.

allow for asymmetry in the logarithmic (base 2) phi-scale of Krumbein (1938), such that the curve can be skewed and the population mean need not coincide with the peak of the curve.

Particle size, shape and density-distribution results. To isolate the effect of particle form on settling velocity, it was attempted to use sediment with an as-narrow-as-possible grain-size distribution, i.e. with the smallest possible standard deviation of particle size. The six sediment populations are (very) well-sorted according to the Folk & Ward (1957) method (Table 3). Grain-size distributions are all slightly skewed towards finer particle sizes (Fig. 7). Size distributions are in accordance with the suitability for the type of experiment they were used in. The particles in the single-grain experiments needed to be sufficiently large to capture in video, while the turbidity-current experiments required sediment fine enough to prevent massive settling of grains in the proximal reach of the flume duct. There is little variation in the distributions of the Corey Shape Factor (CSF), with a mean value of $CSF = 0.56 \pm 0.17$ (mean \pm standard deviation, Table 3), which lie in the range of values reported for carbonate grains in other studies (e.g. Smith & Cheung, 2003: 0.56 ± 0.17 ; Alcerreca *et al.*, 2013: 0.61 ± 0.15 ; Wang *et al.*, 2018: 0.65 ± 0.12 ; Riazi *et al.*, 2020: 0.50 ± 0.14). Corey Shape Factor distributions are slightly skewed towards higher values (Fig. 7). Solid density (i.e. density of the carbonate minerals excluding skeletal macroporosity) was determined for the 204 individual grains used in the single-grain experiments. The one-sigma spread around the mean density is 2.57 to 2.83 mg mm^{-3} (Fig. 8). These values agree with the density of carbonate particles reported in the literature (see De Kruijf *et al.*, 2021, for a compilation). The dependence of settling velocity on particle form can only be investigated if there is no undesired correlation between particle form and the nominal diameter. Cross-plotting of the CSF against the nominal diameter indeed confirms that particle form is not a function of particle size (or mass) for the sediments used in the experiments (Fig. 9).

Experiment setups

The experiments were conducted at the Eurotank Flume Laboratory at Utrecht University, The Netherlands. Tap water was used in all experiments. Water temperature was measured prior to each experiment and was always between 15°C and

17°C; in line with the ambient air temperature at the facility. All experiments were recorded using a high-resolution video camera (Panasonic HC-VX870 4K; Panasonic, Osaka, Japan) with a frame rate of 90 frames per second.

Setup of single-grain settling experiments

The settling tube is a 200 cm tall, transparent polycarbonate pipe of 40 cm diameter (Fig. 10A). The tube was placed vertically in a dark room with a single light source at the top to ensure suitable lighting conditions in the videos. A total of 204 single grains (Table 1) were individually released using tweezers at the top of the settling tube after 5 s of subaqueous wetting to break the fluid surface tension and allow air bubbles to escape open cavities, which is common practice in this type of settling experiment (Maiklem, 1968; Smith & Cheung, 2003; Joshi *et al.*, 2014). Grains were video-recorded along a 50 cm long trajectory between two markers placed 50 cm and 100 cm below the top of the water surface. This trajectory was sufficiently deep to ensure that grains reached terminal settling velocity before reaching the measurement section. Two cameras positioned at right angles in plan view were used to monitor distance from the tube wall and to reconstruct settling trajectory. The cameras were placed perpendicular to the tube at a height precisely between the two markers. Cameras were set to two times optical zoom to minimize perspective distortion, which was verified by a constant running-average vertical velocity over the entire recorded trajectory obtained with automated particle velocimetry using a MATLAB script. Grains that came within 10 cm from the tube wall, as verified using the two perpendicular videos, were discarded to ensure that side wall effects could not affect the recorded settling velocities. The majority of the particles followed a spiral trajectory with a diameter of a few centimetres at most. The centre line of the spiral trajectories was straight vertical to slightly inclined for most particles. Settling paths and temporal velocity variations have been recorded and analysed and will be reported in a follow-up publication. In the present paper, only the average vertical component of the settling velocity is considered, which was calculated using the settling time between the markers. This time was obtained from the high-speed camera footage with a precision of *ca* 0.015 s. After settling, each of the grains was recovered from the bottom of the tube. Grains were dried before fixing into a cup

Table 3. Grain-size distribution of the sediment populations used in the experiments.

Experiment series	Sediment population	Mean grain size*			Grain-size sorting (standard deviation)			Form parameterization	
		Folk & Ward method [†]	Normal-gamma PDF [‡]		Folk & Ward method [§]	Normal-gamma PDF [¶]	Descriptive	Corey Shape Factor (CSF)	Standard deviation
			μ (phi)	μ (mm)					
Single grains	SG-finer	0.08	0.08	0.94	Coarse sand (upper bin)	0.23	0.25	Very well-sorted	0.57
SG-coarser	SG-coarser	-0.85	-0.84	1.80	Very coarse sand (upper bin)	0.20	0.20	Very well-sorted	0.55
Suspension clouds	SC-finer	0.39	0.39	0.76	Coarse sand (upper bin)	0.38	0.39	well-sorted	0.55
SC-coarser	SC-coarser	-0.32	-0.32	1.24	Very coarse sand (lower bin)	0.20	0.23	Very well-sorted	0.55
Turbidity currents	TC-finer	2.50	2.37	0.19	Fine sand (upper bin)	0.60	0.51	Moderately sorted	0.54
TC-coarser	TC-coarser	1.16	1.09	0.47	Medium sand (upper bin)	0.32	0.26	Very well-sorted	0.58

* Phi-scale of Krumbein (1938): $\phi = -\log_2 D_n$, with D_n in mm. [†] Mean of Folk & Ward (1957): $\phi_{\text{mean}} = \frac{\phi_n + \phi_{50} + \phi_{94}}{3}$. [‡] Mean of normal-gamma probability density function, calculated with shape parameter (a) and a scale parameter (b) as $\mu = a \cdot b$. [§] Inclusive Graphic Standard Deviation of Folk & Ward (1957): $\phi_{\text{st.dev.}} = \frac{\phi_{94} - \phi_{16}}{4} + \frac{\phi_{85} - \phi_{15}}{6.6}$. [¶] Sorting (i.e. standard deviation) of normal-gamma probability density function, calculated with shape parameter (a) and a scale parameter (b) as $\sigma = \sqrt{a \cdot b}$.

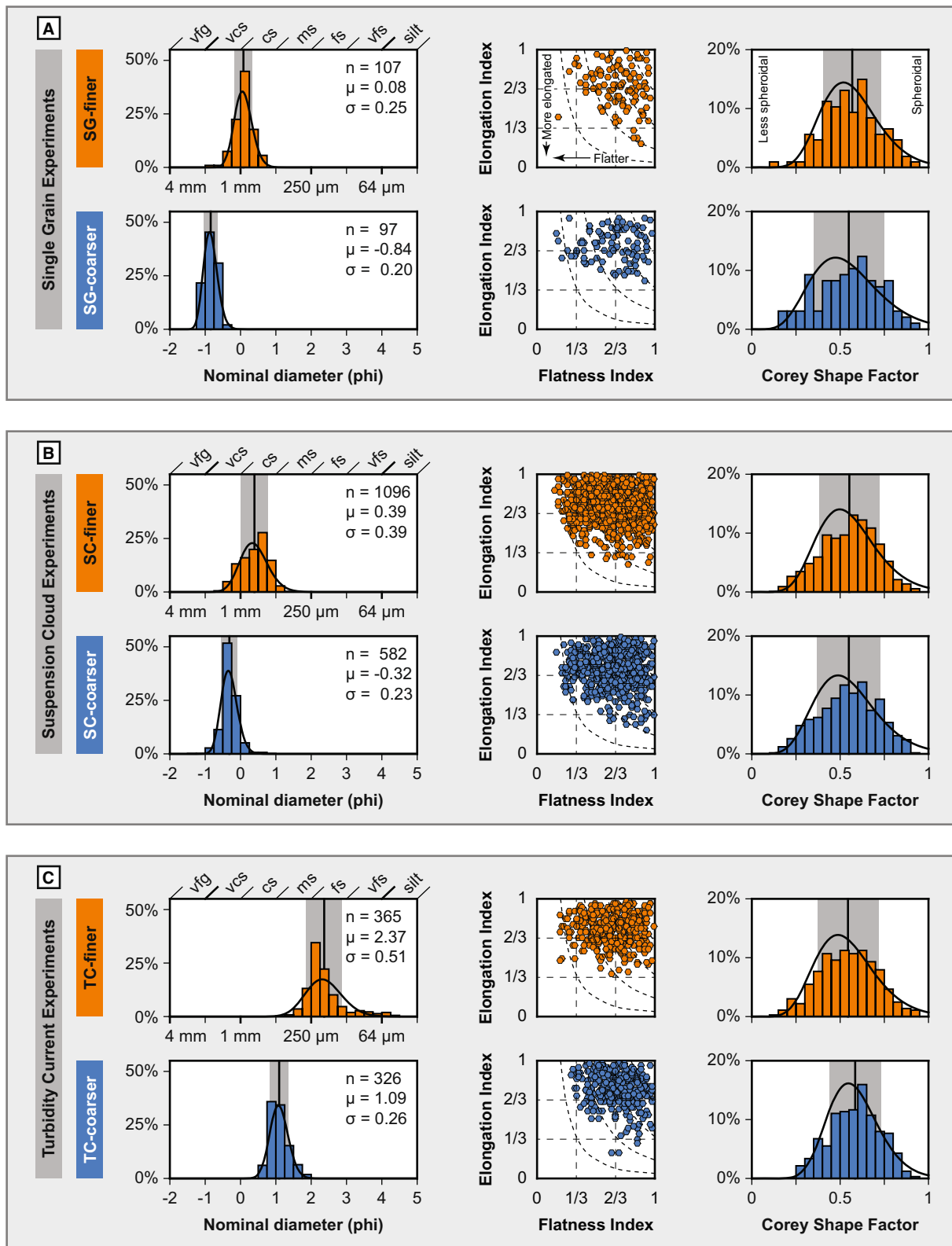


Fig. 7. Grain-size distribution, Zingg diagram and Corey Shape Factor (CSF) distribution of the used sediment populations. Black vertical line and shaded area represent the mean (μ) \pm one standard deviation (σ). Probability density functions (PDFs) are normal-gamma distributions. The curves are slightly skewed towards finer grain sizes and towards higher CSF values.

Fig. 8. Histogram and probability density function (PDF) of solid density for the two populations used in the single grain experiments. Normal-gamma distribution is reported. Black vertical line and shaded area represent the mean (μ) \pm one standard deviation (σ).

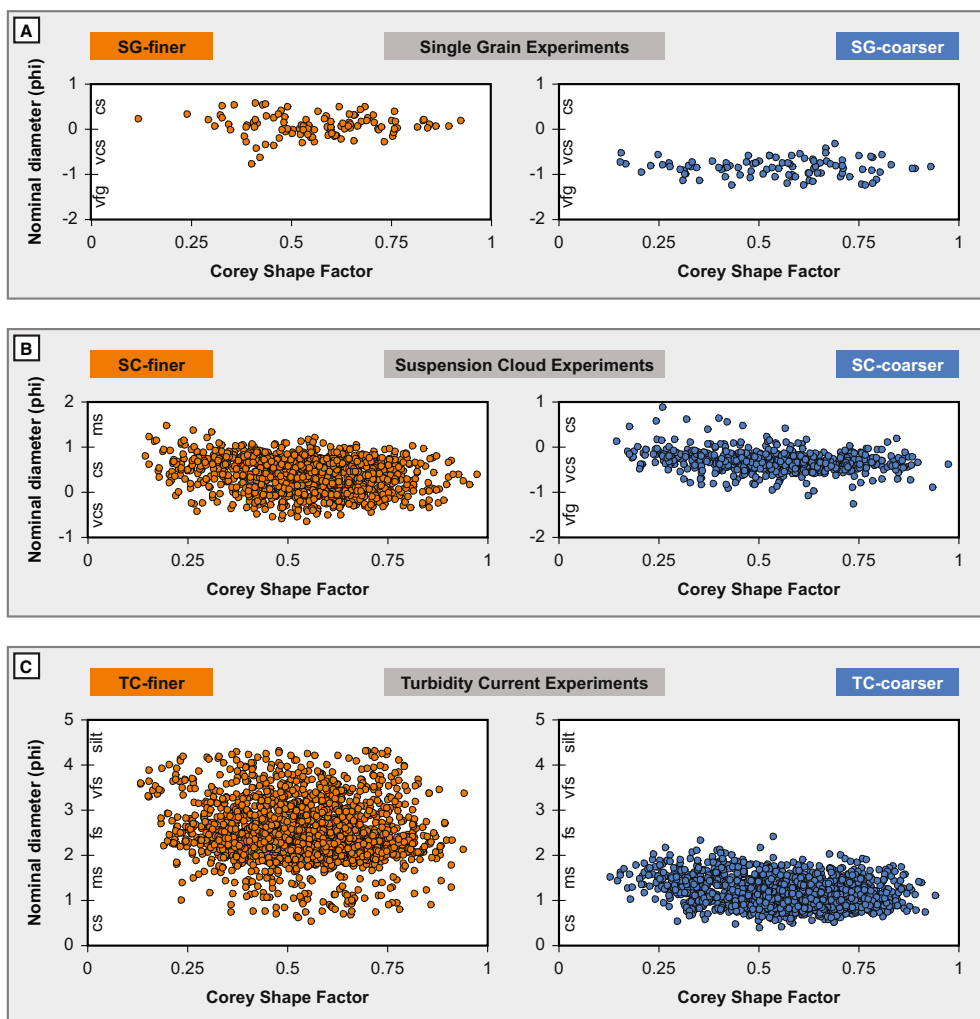
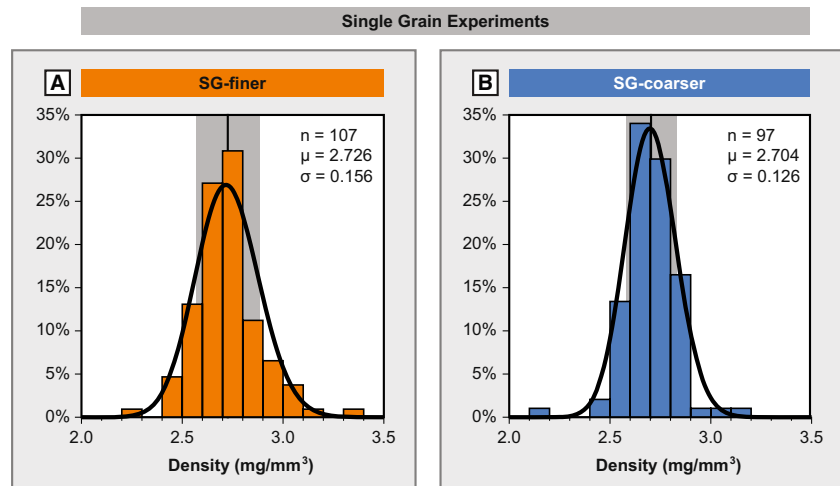


Fig. 9. Shape versus grain size. There is no dependence of grain size on particle form (in terms of Corey Shape Factor – CSF), which confirms that the sediments are suitable for the investigation of a relationship between particle form and settling velocity. All graphs are displayed at the same axis scale to allow for an unbiased comparison between populations.

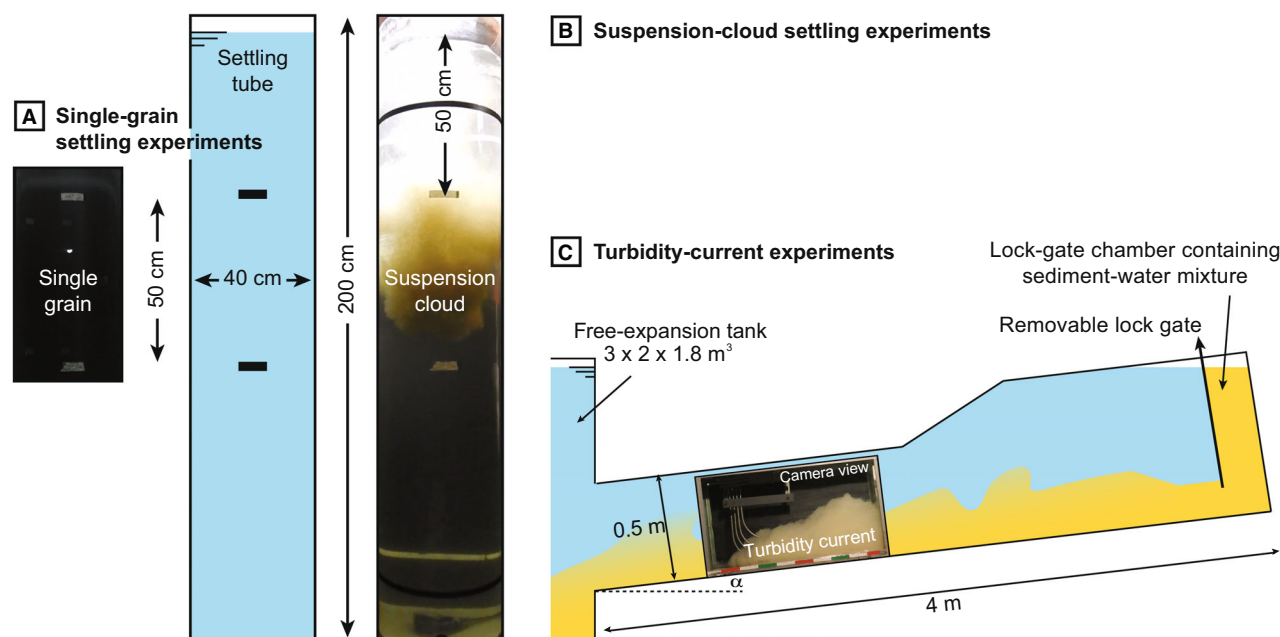


Fig. 10. Experimental setups. A transparent settling tube was used for the (A) single-grain and (B) suspension-cloud settling experiments by the release of sediment at the top of the water column. (C) The turbidity-current experiments were carried out in a submerged, tiltable flume. The sediment–water mixture was prepared in the lock-gate chamber, which was suddenly opened to release the mixture.

of epoxy resin for the micro-CT analysis discussed above. Individual grains were linked to the video recordings in a database. Time intervals between settling runs were sufficient to let the water column come to rest prior to the next run and thus to ensure absence of flow structures that may otherwise have affected the settling velocity of subsequent particles.

Setup of suspension-cloud experiments

Two suspension-cloud experiments were conducted in the same tube as used for the single-grain experiments. One experiment consisted of the settling of 1000 ml of coarse sand (population SC-finer) and the other of 750 ml of very coarse sand (population SC-coarser; volume including *ca* 40% porosity between the grains). Suspension-cloud settling experiments were performed by the sudden release of a beaker filled with water-saturated sediment at the top of the tube (Fig. 10B; Videos S1 and S2). The quantity of sediment was kept low to attempt maintaining low sediment concentrations within the suspension cloud with the aim to achieve limited particle–particle interactions. In this way, grains would settle relatively freely such that sediment sorting is largely controlled by particle segregation due to differential settling velocities along the 200 cm

deep falling path. The suspension clouds each generated a 2 to 3 cm thick deposit at the bottom of the tube, which was collected using a cup of 8 cm diameter placed at the centre of the tube floor prior to each experiment. After drying of the sediment in the cup, horizontal slices of the deposit were sampled using adhesive tape. Twenty sample layers for population SC-finer and ten layers for SC-coarser comprised the entire deposit. Hundreds of grains subsampled from a selection of these layers were fixed into epoxy resin for micro-CT analysis (Table 1).

Setup of turbidity-current experiments

A tiltable flume duct of 400 cm long, 20 cm wide and 50 cm deep, entirely filled with water was used for the dilute turbidity-current experiments (Fig. 10C; Video S3). At the upper end of the apparatus, a sediment–water mixture was prepared in a closed compartment of 50 l volume with a removable lock gate. Sediment was brought into suspension using a water jet at the bottom of the compartment. The closed compartment contained 2000 ml of carbonate sand for the TC-finer experiment and 3000 ml for the TC-coarser experiment. These volumes include *ca* 40% porosity such that the net sediment concentration in the compartment prior to the release of sediment at the start of the

experiments was *ca* 2.4% and 3.6% by volume, respectively. As for the suspension-cloud experiments, it was attempted to keep sediment concentrations low, trying to ensure the free settling of sediment grains. Upon the sudden opening of the removable lock gate, a dilute turbidity current travelled down the slope. The bottom of the lock-gate chamber consisted of a ramp that was steeper than the flume floor (*ca* 30° from the horizontal) to aid the initial acceleration of the current. The floor of the duct consisted of smooth polycarbonate material. After leaving the duct, flows could expand in a *ca* 12 m³ tank preventing a reflection wave at the density interface from interfering with the current. Two experiments were conducted using two different sediment populations (Table 3). Test runs revealed that a slope angle of 1° for sediment population TC-finer and 8° for TC-coarser created a deposit over the entire length of the flume floor, without significant deposition on the steeper ramp in the mixing compartment and without significant amounts of sediment being flushed into the expansion tank at the end of the duct. After each experiment, the duct was carefully drained to prevent sediment transport disturbing the deposit. Sediment samples were then collected by scooping from three stations at proximal, intermediate and distal positions along the flume floor at 30 cm, 155 cm and 280 cm downslope from the lock gate. Samples were dried and fixed into epoxy resin for micro-CT analysis (Table 1).

RESULTS

Results of single-grain settling experiments

In the single-grain (SG) settling experiments it was investigated whether there is a relationship between settling velocity and particle shape. The terminal settling velocity of 107 grains of SG-finer and 97 grains of SG-coarser has been recorded and plotted in histograms (Fig. 11). Settling-velocity is normal-gamma distributed with a slight skew towards higher velocities. Settling velocities are in the range of 0.05 to 0.12 m/s in SG-finer and 0.06 to 0.20 m/s in SG-coarser (corresponding mean particle Reynolds numbers and standard deviation: $Re_p = 79 \pm 26$ in SG-finer, $Re_p = 219 \pm 78$ in SG-coarser, see datasheet in [Supplementary Materials](#)). Grains settle between 50% slower and 50% faster than the population-average velocity (i.e. fastest particles are about three times faster than slowest ones). Cross-plots of density, grain size and particle-form

parameters are shown in Fig. 12. The observed spread in settling velocity is not due to variation in particle density; in SG-coarser the effects of other variables even produce a negative correlation between settling velocity and density. As expected, settling velocity partly depends on grain size, but is significantly influenced by shape parameters as evidenced by the scatter. The correlation between settling velocity and the various shape parameters is stronger in SG-coarser than in SG-finer (Fig. 12), because the effect of grain size on settling velocity is more important in SG-finer. Elongation does not influence settling velocity much. Corey Shape Factor (CSF) and flatness show the strongest statistical correlation with settling velocity (Fig. 12).

Grain size and particle form, in SG-finer and SG-coarser, are independent of one another (Fig. 9A). In Fig. 13A data points of particle form against grain size are colour-coded with the difference from the population-average settling velocity, such that green data points indicate the faster particles and red points the slower ones. The horizontal colour gradient in the diagram of SG-coarser emphasizes the correlation between settling velocity and CSF. In the diagram of SG-finer, however, the colour gradient is significantly affected by grain size. Therefore, the grouping of similar settling velocities between CSF isolines in the Zingg diagram is more pronounced in SG-coarser than in SG-finer (Fig. 13B). The Zingg diagram also shows that flatness exerts a stronger control on settling velocity than elongation. Thus, the fastest-settling particles within a narrow grain-size range are spheroids and rods. Discoids and blades settle at lower velocities. It is shown that differential settling velocity becomes more pronounced as grain size increases.

Results of suspension-cloud settling experiments

In the suspension-cloud experiments it was tested whether the shape-dependent settling-velocity trends observed in the single-grain experiments yield a sorting mechanism in suspension deposits. At terminal velocity, the base of the suspension cloud travelled at *ca* 0.20 m/s for both populations. The body of the cloud took 10 s to pass the lower marker (1 m below the tube top) in SC-finer and 7.5 s in SC-coarser. The tail passed the marker about 15 s and 25 s later, respectively. It took just over a minute for the final grains to reach the bottom of the column (Videos S1 and S2).

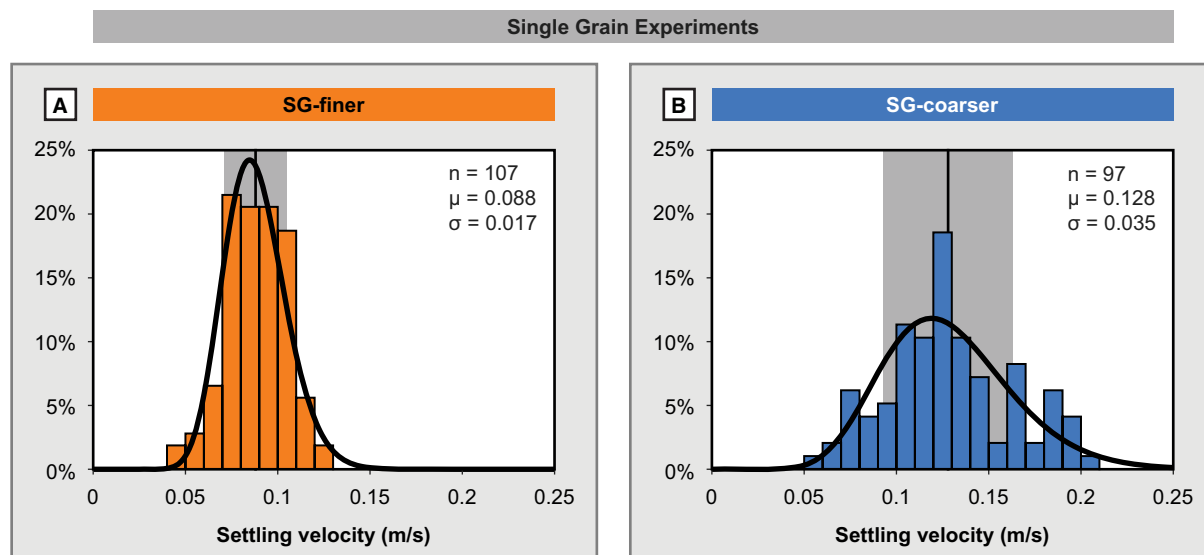


Fig. 11. Single-grain settling experiments. Histogram and probability density function (PDF) of normal-gamma distribution of terminal settling velocity. Black vertical line and shaded area represent the mean (μ) \pm one standard deviation (σ).

Most of the variation in any of the parameters occurs at the base and towards the top of the deposits, whereas in the central part of the deposits the parameters are more uniform (Fig. 14). For both populations, particles become smaller, less spheroidal (CSF), flatter, slightly more elongated, and less equant from base to top. Most notable is the difference in grain-size variation. The SC-finer deposit fines upward with almost one phi unit from very coarse sand. In SC-coarser, grain size decreases upward with only 0.5 phi from upper to lower very coarse sand. These different vertical grain-size sortings in part reflect grain-size distributions of the bulk sediments, which was wider in SC-finer than in SC-coarser (Fig. 7; Table 3). Absence of grain-size variation would have otherwise isolated the effects of particle form on the sorting mechanism within the sinking suspensions, because as grain size increases the influence of particle shape enlarges and may become dominant in controlling velocity-dependent sediment sorting. Therefore, although shape-parameter trends are comparable between the two populations, the upward decrease of shape-indices is stronger in SC-coarser than in SC-finer due to the narrower grain-size sorting in SC-coarser. Similar to observed in the single-grain settling experiments, the role of grain size is more significant for the finer population.

In the SC-coarser deposit, the Corey Shape Factor, flatness and equancy indices decrease

upward with 29%, 24% and 33%, respectively (Fig. 14). The PDFs become slightly less sharp upward (wider distributions) for flatness and slightly sharper upward (narrower distribution) for equancy. Particle elongation shows little variation, except for the bottom sample, which contains less-elongated particles.

Vertical variation in particle shape is also plotted in Zingg diagrams (Fig. 15). The distribution of data points in each of the 'difference diagrams' shifts towards less spheroidal shapes (away from top right corner) with lower CSF values (isolines). Because the particles plot mostly in the upper half of the Zingg diagram, this shift takes place dominantly along the horizontal flatness-axis as particles morph from largely spheroidal (red shades) to discoidal (green shades). The strongest increase in the proportion of rod-shaped particles, and to a lower extent in that of blades, occurs at the base of the deposit as indicated by the green shades in those regions of the Zingg diagram. Sorting in suspension clouds thus mimics the trends observed in the single-grain experiments.

Results of turbidity current experiments

These turbidity current (TC) experiments explored for a sorting mechanism in carbonate turbidity currents by differential shape-dependent settling velocities of individual grains. Sediment

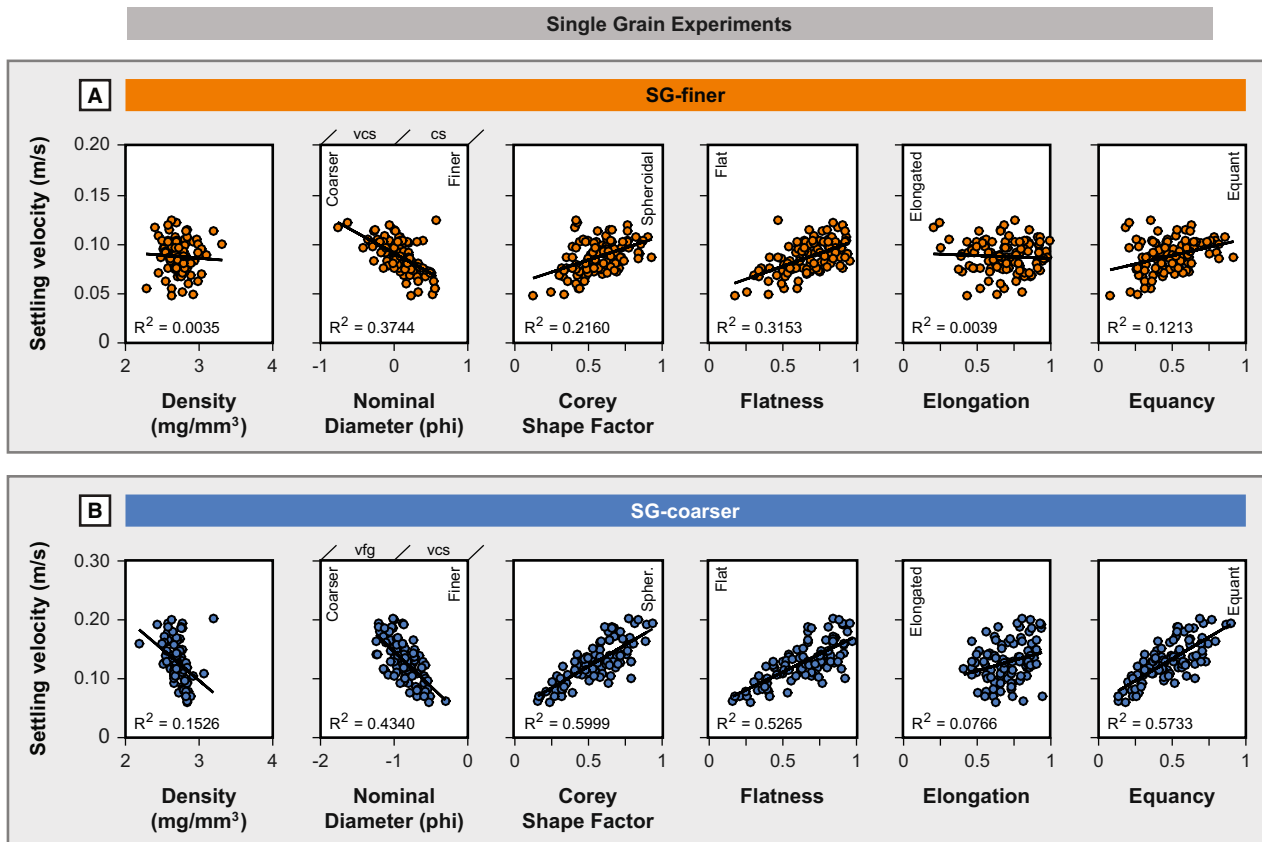


Fig. 12. Single-grain settling experiments. Terminal settling velocity against solid particle density, nominal particle diameter and various shape parameters. The variation in settling velocity is not explained by differences in density. Settling velocity is partly influenced by grain size. Flatness, equancy and Corey Shape Factor show higher correlation with settling velocity. Linear trendlines are displayed.

populations TC-finer and TC-coarser were used, which are relatively fine-grained to maintain particles in suspension long enough for deposition over the full length of the flume without entirely bypassing into the expansion tank, for which the flume slope and sediment concentrations in the mixing compartment were adjusted accordingly. The head of the TC-finer turbidity current moved with an average velocity of 0.08 m/s (Video S3). The TC-coarser turbidity current had an average head velocity of 0.05 m/s. Both turbidity currents were turbulent (Reynolds numbers = $1\text{--}2 \times 10^4$). From the lock gate to the distal station, sediment concentrations dropped as visually observed from decreasing opacity with distance.

Sediment was collected at three longitudinal stations along the flume floor. Particle-size analysis reveals that both turbidites are fining distally (Fig. 16). In the TC-finer turbidite, grain size drops with half ϕ (from lower medium to upper fine sand) from the proximal to the intermediate station and with a full ϕ unit (from upper fine to upper

very fine sand) from intermediate to distal. For the TC-coarser turbidite, grain size is similar between proximal and intermediate stations (lower coarse sand), and drops half a ϕ unit from intermediate to distal (from lower coarse to upper medium sand). Like in the other experiments, the influence of particle form on the sediment sorting mechanism is more pronounced for coarser grain sizes. Because both populations are relatively fine-grained, the variation in particle-form indices is small. The dominant effect of grain size on the settling velocity of small particles, therefore, is reflected in the significant distal fining of the TC-finer turbidite, which flattens out the longitudinal variation in shape parameters (Fig. 16A). Distal fining is less pronounced, though not absent, in the TC-coarser turbidite with the result that variation in shape parameters is strongest for this population.

The distal fining of the TC-finer turbidite is too significant for the particle-form indices to yield insights about a shape-dependent sorting mechanism in carbonate turbidity currents. The

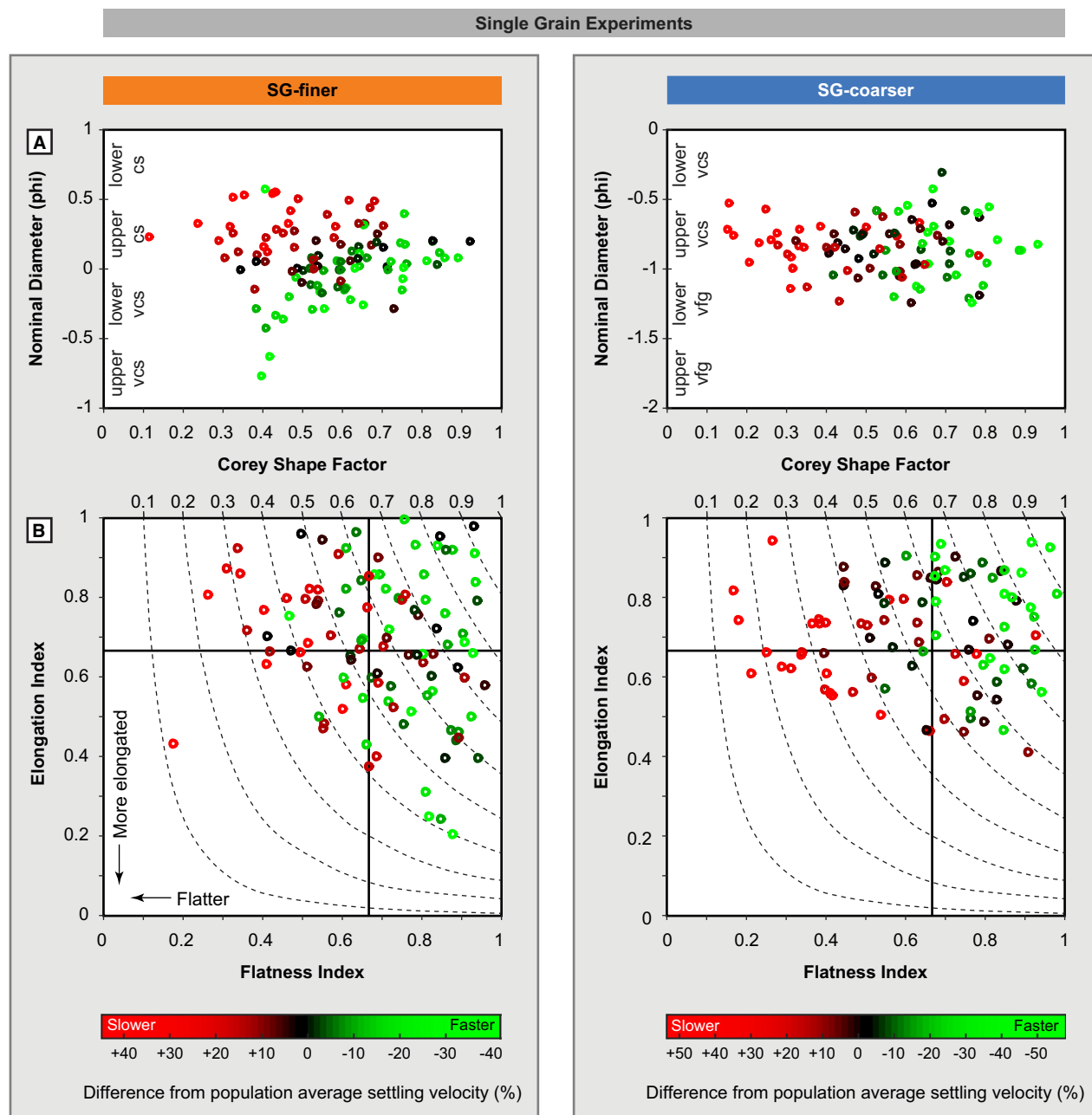


Fig. 13. Single-grain settling experiments. (A) Particle form (Corey Shape Factor – CSF) against grain size. Same data as in Fig. 9, but here colour-coded with terminal settling velocity relative to the population average. Settling velocity increases with CSF. However, in population SG-finer the data are not free of a grain-size dependency. (B) Terminal settling velocity in the Zingg diagram. Plotted values are relative to the population average.

difference diagrams that were calculated by subtracting particle counts in the different shape classes of the Zingg diagram, therefore, do not produce useful results in TC-finer (Fig. 17A). The TC-coarser turbidite, on the other hand, has values of Corey Shape Factor, flatness and equancy that decrease from proximal to distal

with respectively 14%, 13% and 14%, with the largest variation between the intermediate and distal stations. There is little variation in elongation. These observations also show in the difference diagrams of TC-coarser, which indicate that particles shift dominantly towards flatter shapes marked with lower CSF values (Fig. 17B).

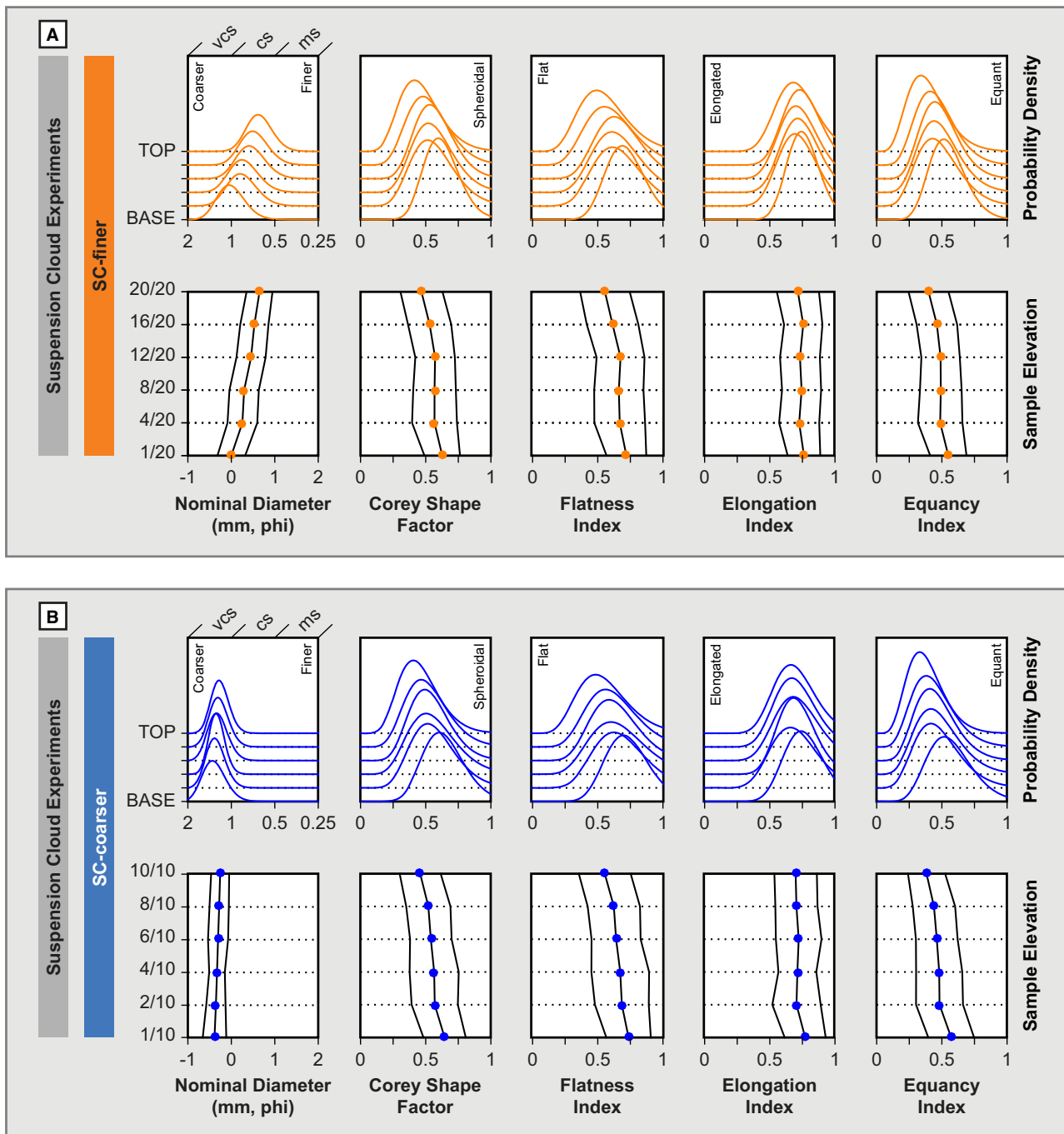


Fig. 14. Suspension-cloud settling experiments. Particle-size and particle-shape distribution through the suspension-cloud deposits. Layers 1/10 and 1/20 are the base; layers 10/10 and 20/20 are the top. Upper rows show probability density functions (PDFs) of normal-gamma distribution based on histogram data (not shown). Lower rows indicate mean (dot) and standard deviation (solid black lines). The SC-finer deposit is fining-upward, which indicates that grain size plays a primary role in sediment sorting and that shape is of subordinate importance in SC-finer. In the SC-coarser deposit vertical grain-size variation is minimal and trends in shape parameters are more pronounced. Corey Shape Factor (CSF) (−29%), flatness (−24%) and equancy (−33%) decrease significantly as grains become flatter and less equant from base to top. There is little variation in elongation.

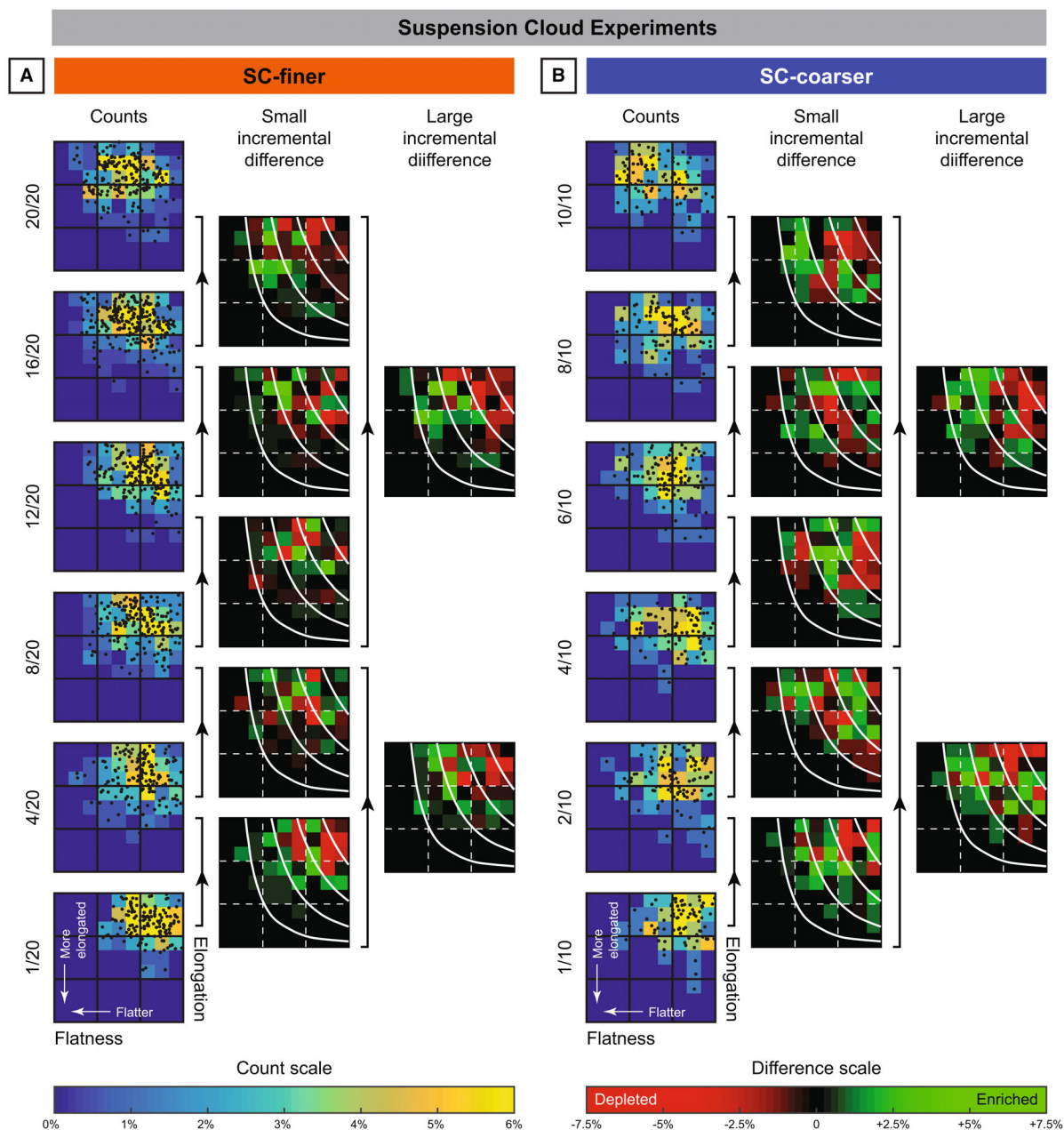


Fig. 15. Suspension-cloud settling experiments. Particle-shape data in Zingg diagrams of vertical samples from the suspension-cloud deposits. Layers 1/10 and 1/20 are the base. Layers 10/10 and 20/20 are the top. The shift in shape-data points between samples is reflected in difference plots (see Fig. 6 for explanation). Green shades indicate enrichment in those shapes, red shades depletion. Some shape classes are over 30% different between samples. Grains become less spheroidal upward as indicated by colour shifts along Corey Shape Factor (CSF)-fields (white isolines).

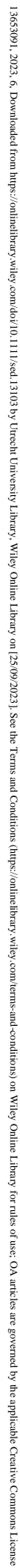
DISCUSSION

Settling of carbonate particles

Settling of a single carbonate grain

The settling of grains in isolation is unhindered by interactions with other grains. single-grain settling

experiments provide information about the terminal fall velocity, of which only the vertical component was analysed here. It was observed that shape parameters display a statistical correlation with settling velocity, which was stronger in the coarser samples (Fig. 12). The experiments showed that the influence of particle shape on settling velocity



15636091, 2023, 6, Downloaded from <https://onlinelibrary.wiley.com/doi/10.1111/psl.13103> by Utrecht University Library, Wiley Online Library on [25/09/2023]. See the Terms and Conditions (<https://onlinelibrary.wiley.com/terms-and-conditions>) on Wiley Online Library for rules of use; OA articles are governed by the applicable Creative Commons License

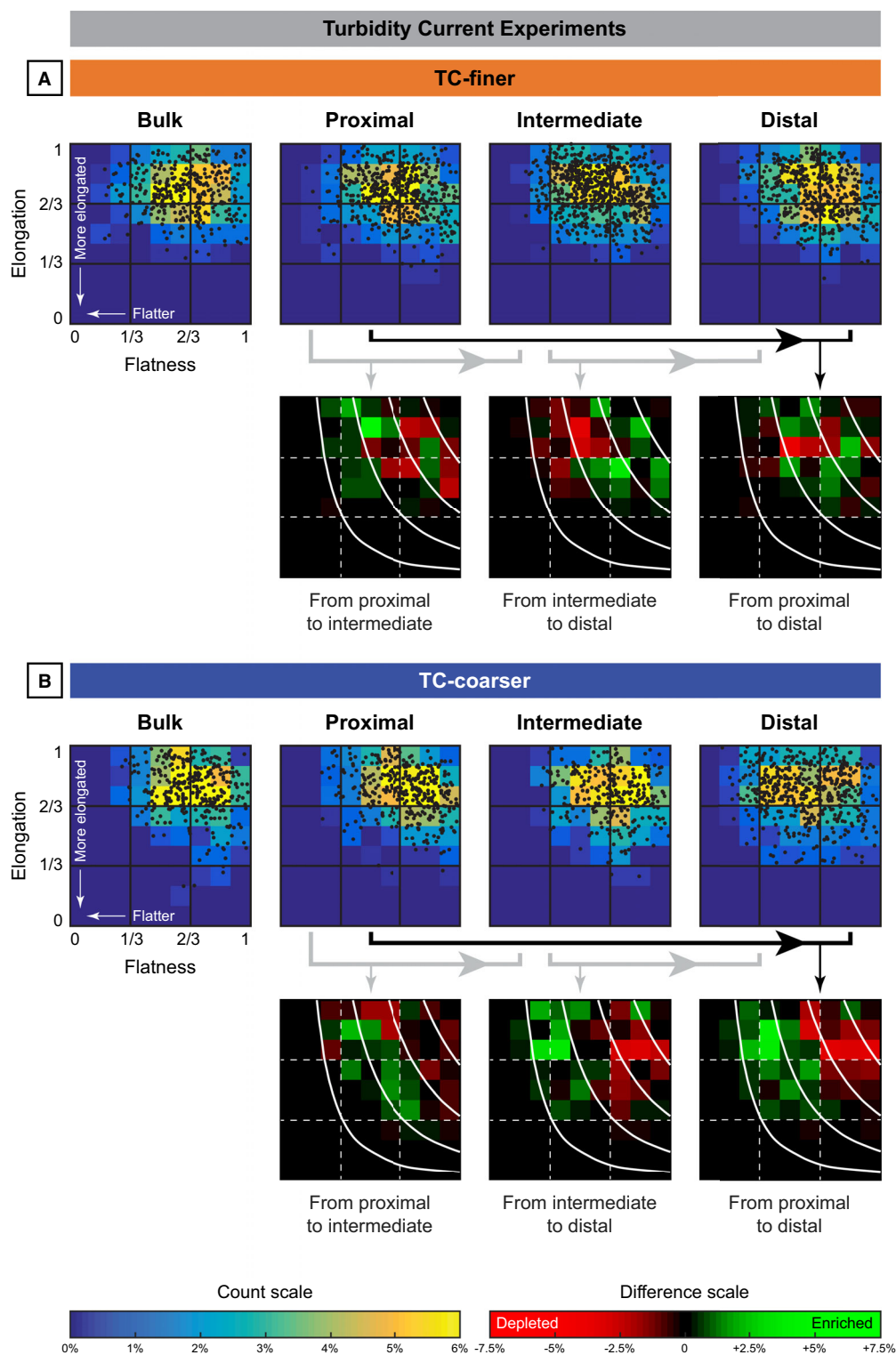


Fig. 17. Turbidity-current experiments. Particle-shape data in Zingg diagrams of longitudinal samples from turbidite deposits. The shift in shape-data points between samples is reflected in difference plots (see Fig. 6 for explanation). Green shades indicate enrichment in those shapes, red shades depletion. Distal fining of the TC-finer turbidite is too significant for the difference diagrams to provide useful insights. Results of TC-coarser are more meaningful because the influence of longitudinal grain-size variation is limited (see Fig. 16). Some shape classes are up to 14% different between samples. Grains become less spheroidal distally as indicated by colour shifts along Corey Shape Factor (CSF)-fields (white isolines).

becomes more significant as grain size increases (see also Komar & Reimers, 1978; Baba & Komar, 1981). This shape dependency can be explained by the width of the shape distribution, which operates on the mean settling velocity for a certain nominal diameter (Fig. 18A). Shape distribution can be expressed as a mean and a standard deviation, which determine a range of probable values in the settling velocity domain. The *relative* effect of shape distribution in the settling-velocity domain, expressed as a percentage, may remain approximately constant over the entire range of particle diameters (confidence envelope). In terms of *absolute* values, on the other hand, the lower settling velocity of smaller grains yields a narrower range of shape distribution in the settling-velocity

domain than for larger grains. As a result, the difference between the fastest and slowest settling particles for a certain nominal diameter becomes progressively larger with increasing grain size (Fig. 18).

The width of the settling-velocity distribution found in the single-grain experiments in this study compares well with other settling studies using skeletal carbonate sands, such as the well-cited dataset of Smith & Cheung (2003; Fig. 18B). Although the present authors do not wish to imply a linear relationship between phi-nominal diameter and particle settling velocity, it serves as a first approximation in the range from medium sand to fine gravel ($R^2 = 0.85$). Because of different scopes of the studies, the range of tested grain sizes is

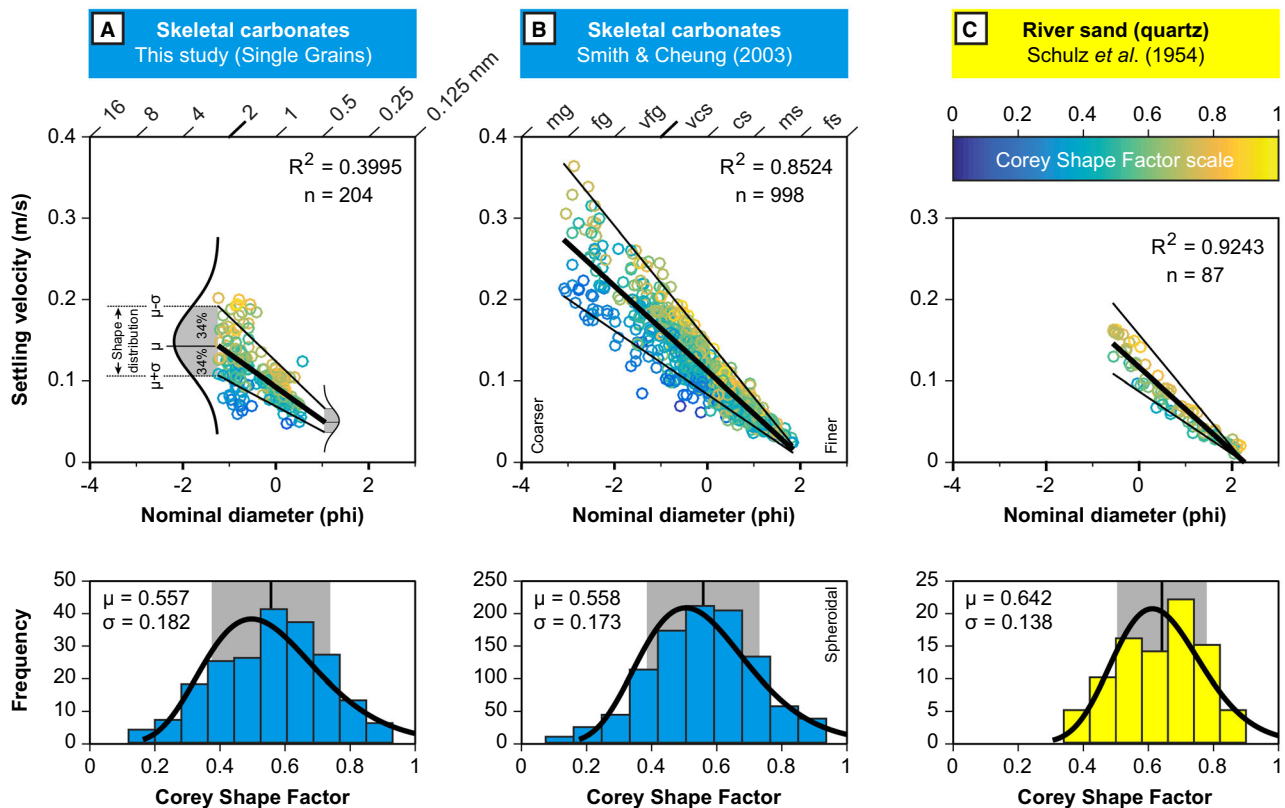


Fig. 18. Comparison of single-grain experiments with other studies. (A) Skeletal carbonates of this study. (B) Skeletal carbonates of Smith & Cheung (2003). (C) Quartz river sand of Schulz *et al.* (1954). Data points are colour-coded with Corey Shape Factor (CSF). Trendlines of linear regression are shown as an approximation. Mean (μ , thick line) and standard deviations (σ , thin lines) are indicated. The vertical distribution of data points (in settling-velocity domain) results from a distribution in particle forms. The relative distribution in settling velocity remains more or less constant (linear trends of confidence envelopes). In absolute values, the range of settling velocities increases as grains become larger, yielding greater variation in settling velocity for larger grain sizes. The degree of scatter is comparable between the skeletal carbonate datasets. The distribution of settling velocity is much smaller for the quartz sand. These differences in the width of the settling-velocity confidence envelope correspond to the distribution in CSF. Extreme particle forms with low CSF values are responsible for the broader distribution of settling velocity in skeletal carbonates.

much larger in the Smith & Cheung (2003) dataset than in this study. The Smith & Cheung (2003) dataset has a steeper linear trendline than the dataset here, which may be due to a difference in grain-size range of respectively 5 phi and 2 phi. However, the tropical origin of the carbonate sand of Smith & Cheung (2003) and the cool-water nature of the sediment used here may also be of influence. Yet, the range of settling velocities for a given grain size is very comparable between the two carbonate datasets. This similarity is rooted in the likeness between the shape distribution of these sediments, as demonstrated in the Corey Shape Factor histograms (Fig. 18). It should be remarked, though, that several carbonate-settling datasets available in the literature contain grains that were selected to represent a range of Corey Shape Factors. Therefore, caution must be exercised when taking such assorted datasets as being representative of natural carbonate sediment populations, because they may be affected by selection bias. The datasets of Smith & Cheung (2003) and this study are composed of large numbers of randomly selected grains and are therefore assumed to represent natural carbonate sediment populations.

There are surprisingly few datasets available on the settling velocity of siliciclastic sand grains for which also the Corey Shape Factor is reported or can be calculated. A positive exception is the study of Schulz *et al.* (1954), who analysed the settling velocities of riverbed quartz sand. Although the range of grain sizes is limited to between -1 phi and 2 phi (medium to very coarse sand), Schulz *et al.* (1954) report 87 data points (Fig. 18C). Compared with the carbonate datasets, there is much less scatter in the quartz dataset, and the one-sigma confidence envelope is narrower accordingly. The reduced width of the settling-velocity distribution for a given particle diameter in the quartz dataset is attributed to the narrower distribution of the Corey Shape Factor in comparison with the carbonate datasets. Note that the quartz river sand is not uniquely spheroidal (irrespective of grain angularity). The values at the upper end of the Corey Shape Factor distributions are comparable between all three datasets ($\mu + \sigma = 0.739$ for this study; 0.731 for Smith & Cheung, 2003; 0.780 for Schulz *et al.*, 1954). The extreme particle forms, marked by lower Corey Shape Factor values, however, are more abundant in the carbonate datasets than in the quartz dataset ($\mu - \sigma = 0.375$ for this study; 0.385 for Smith & Cheung, 2003; 0.504 for Schulz *et al.*, 1954). The presence of extreme particle forms (platy, bladed and elongated) in the skeletal carbonate sediments

explains why the within-sample spread in settling velocity is larger than for the quartz sand.

Bulk settling of sediment suspensions

Sediment particles that settle in groups have more complicated hydrodynamics than grains that settle in isolation (Hulsey, 1961; Davies, 1968). The established model for the settling of suspension clouds is based on previous experiments using glass beads and quartz sand in very wide water tanks. The model encompasses three stages: (i) initial acceleration; (ii) thermal stage; and (iii) swarm stage. After release, particle clouds undergo widening and volumetric increase by fluid entrainment due to shear between the boundaries of the cloud and the ambient water (Scorer, 1997). After the initial acceleration stage, the irregular-shaped cloud transitions into the thermal stage, in which sediment particles and interstitial water move downward together (Turner, 1973; Bühler & Papantoniou, 2001). In this stage, the cloud behaves as a vertical particulate gravity current. As the settling velocities of individual particles exceed about one-third of the settling rate of the whole cloud, the now bowl-shaped suspension shifts into the swarm stage (Moghadari-pour *et al.*, 2017). In this regime, the turbulent kinetic energy of particles is dissipated and interstitial fluid remains nearly motionless as particles rain vertically through it (Bühler & Papantoniou, 2001). Suspension-cloud experiments using skeletal carbonates have to date only been performed by Chen *et al.* (2022), who found that the above model also holds for carbonate suspensions.

In the experiments in this study, the skeletal carbonate clouds started interacting with the side walls of the tube soon after release (Videos S1 and S2). The thermal stage, in which the cloud moved downward as a vertical turbidity current, was therefore not fully developed. However, about the time the first grains reached the bottom of the tube, the dynamics of the clouds resembled the swarm stage. As the clouds settled, suspended grains attained different settling velocities within the sinking cloud, yielding a sediment sorting process. This sorting mechanism was potentially affected by particle interferences, such as collisional encounters and upward water displacement, which obstruct the free settling of grains. Although these effects are especially significant at elevated concentrations of suspended sediment (Richardson & Zaki, 1954; Thacker & Lavelle, 1977; Baas *et al.*, 2022), some considerations are presented here with particular focus on irregular grains.

The frequency of collisional encounters between particles is a function of volumetric

sediment concentration (Bagnold, 1954; Cheng, 1997; Baldock *et al.*, 2004), as well as the settling trajectory of individual particles (Jenny *et al.*, 2004; Veldhuis & Biesheuvel, 2007; Uhlmann & Doychev, 2014). Free-settling skeletal carbonate grains tend to follow irregular paths (Maiklem, 1968; Braithwaite, 1973) and are therefore susceptible to hitting other particles at a higher rate than spheroidal grains that tend to fall along near-straight vertical trajectories (Clift *et al.*, 1978; Mathai *et al.*, 2018). Particle–particle collisions may hamper a grain shape-dependent sorting mechanism.

Particles that settle in the vicinity of other grains are also affected by the turbulence generated around those sinking grains (for example, the wake effect; Murray, 1970; Nielsen, 1993; Liang *et al.*, 1996). The fluid that is displaced upward as grains move down through the water column generates additional drag that reduces the effective settling velocity of particles, a process referred to as hindered settling (Kermack *et al.*, 1930; Richardson & Zaki, 1954; Baas *et al.*, 2022). Hindered settling is classically predicted by the equation of Richardson & Zaki (1954), which went through numerous modifications to adapt it for sediment mixtures in terms of grain size, density and shape (Masliyah, 1979; Cheng, 1997; Kumbhakar *et al.*, 2017; Spearman & Manning, 2017; Baas *et al.*, 2022). Hindered settling is enhanced as grains become more irregular, but is reduced as grain size increases (Fouda & Capes, 1977; Tomkins *et al.*, 2005). Sphericity-based fluid drag models do not capture the complexity of skeletal grain morphologies, requiring drag coefficients for multi-particle arrangements of carbonate grains (Wang *et al.*, 2018). The improved equation of Baas *et al.* (2022) is used here to evaluate the effect of hindered settling in the suspension-cloud experiments in this study. Based on particle Reynolds numbers of sediment used in the single-grain experiments, it is assumed that also the particles in the suspension-cloud experiments settled in the transitional regime ($10 < Re_p < 500$). Sediment concentrations have not been quantified, but it is estimated that concentrations did not exceed 5% by volume and were likely much lower. At sediment concentrations of 2%, 3.5% and 5%, settling velocities are reduced to, respectively, 95%, 90% and 85% of the settling velocity in clear water (eq. 5c of Baas *et al.*, 2022). These values demonstrate that the effects of grain-size and shape were

dominant over hindered settling in controlling settling velocity.

Shape effects were observed in the experiments performed here. Similar to the single-grain experiments, shape sorting becomes more explicit as grain size increases. The effect of the sorting mechanism in carbonate sediment suspensions, thus operating through shape-dependent settling velocities, is illustrated in Fig. 19. This conceptual model applies to suspension fallout of sediment particles in a narrow grain-size range. Typical skeletal components corresponding to the different Zingg-shape classes are given in Table 4. For both experiments, the rate of change in grain size and any of the shape parameters was largest for the samples collected from the bottom and top of the deposits, which is interpreted as a result of processes obstructing the free settling of particles as if in isolation. Both SC-finer and SC-coarser suspension clouds showed a downward frontal velocity of *ca* 0.20 m/s. These maximum velocities coincide with the highest settling velocities observed in the single-grain experiments. The slowest grains in the tail of the suspension took about 1.5 times longer than expected on the basis of the slowest grains in the single-grain experiments. At the base of the sand suspension, segregation was due to fast particles ‘outrunning’ the slower grains in this region of the cloud. Similarly, slow particles in the upper part of the suspension were ‘left behind’ in the tail as the body sank through the tube. Slow particles at the base were obstructed to move upward through the cloud in the same way that faster particles were not able to sink from the top into the lower regions of the cloud. Thus, suspended particles prevented the segregation of grains according to their settling velocity to some degree (see also Masliyah, 1979; Cheng, 1997; Kumbhakar *et al.*, 2017; Spearman & Manning, 2017).

Settling in turbidity currents

Turbidity currents are essentially sediment suspensions with an effective downslope velocity due to excess density compared to the ambient water (Kuenen, 1937; Johnson, 1939). Fluid turbulence is the main particle-support mechanism in turbidity currents, counteracting the effect of gravitational settling of sediment grains. The effect of differential settling velocities between grains on the distribution of grain size, particle density and particle shape in calciturbidites is the focus of this section. Previous turbidity-current experiments using natural carbonate sediments focused on

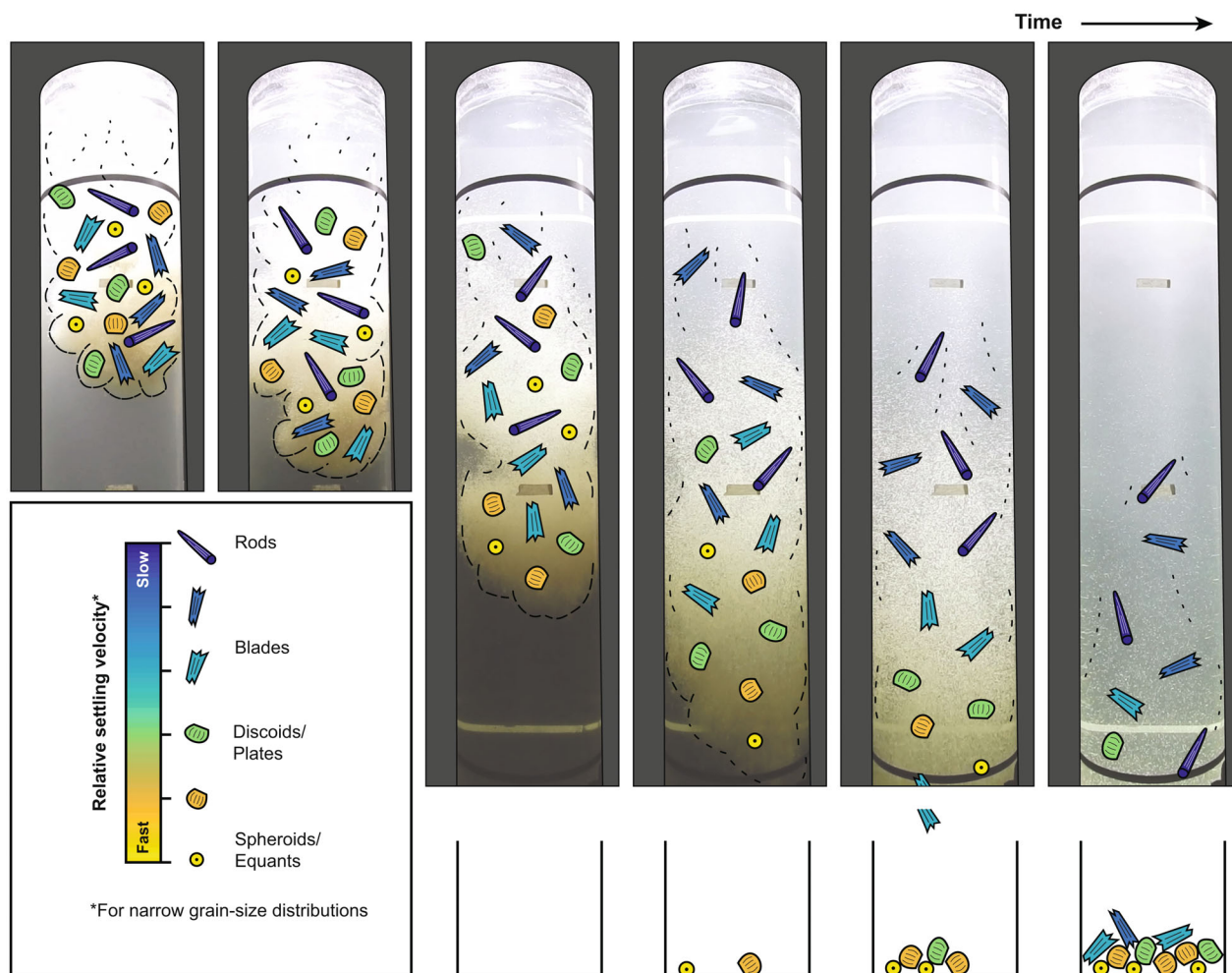


Fig. 19. Shape sorting in carbonate sand suspensions. Interpretation of the particle-shape fractionation mechanism due to differential settling velocities. Drawn over the photographs of the SC-coarser experiment from Fig. 14. Grains with the highest settling velocities concentrate towards the base, whereas the lowest settling-velocity particles move preferentially towards the top of the cloud. The combination of grain size, density and particle shape controls settling velocity. For narrow ranges of grain size and density, the effect of shape sorting was observed. Shape sorting becomes increasingly significant for larger grains. Particle-particle interactions may hamper the sorting process. See Table 4 for typical compositions of grain shapes.

the hydrodynamic behaviour of foraminifera (Kelham, 2011; Ash-Mor *et al.*, 2022a) and coccoliths (Buls *et al.*, 2017). Rather than concentrating on composition-specific grains, the present experiments investigated a representative population of natural skeletal carbonate sand. The sorting of particles according to their hydrodynamic properties is referred to as *hydraulic sorting*, which, in the context of turbidites, can be interpreted as the distribution of settling velocity (Bornhold & Pilkey, 1971; van Tassell, 1981; Sadler, 1982; Komar, 1985). The relationship between settling velocity and grain size, particle density and particle shape in the context of turbidites is discussed here. The

effect of cohesive sediments on sorting in turbidity currents (e.g. Baas *et al.*, 2009, 2011) is beyond the scope of the present contribution, which focuses exclusively on non-cohesive turbidity currents composed of sand grains.

Grain size. The relationship between grain size and settling velocity is deeply rooted in the turbidite model, explaining the origin of graded bedding (Kuenen & Migliorini, 1950) and the distal fining of lobe deposits (Bouma, 1962). Hydraulic sorting of different grain sizes has been experimentally investigated using the release of polydisperse suspensions in rectangular flume setups

Table 4. Typical skeletal and non-skeletal grains of the four shape classes of the Zingg diagram.

Spheroids	Discoids	Blades	Rods
Ooids	Bivalves	Bivalves	Echinoid spines
Corals	Brachiopods	Brachiopods	Red algae
Red algae	Echinoid plates	B. foraminifera	Bryozoa
P. foraminifera	Bryozoa	Echinoid plates	Gastropods
B. foraminifera	Crinoid columnals	<i>Halimeda. Sp</i>	
Faecal pellets	<i>Halimeda. Sp</i>		
Aggregates	B. foraminifera		

Based on literature compilation of available experimental studies on the settling of marine carbonate grains (De Kruijf *et al.*, 2021). This list is not conclusive: breakdown of skeletons may produce a wide variety of forms.

(Middleton, 1967; Gladstone *et al.*, 1998; Marr *et al.*, 2001; Choux & Druitt, 2002; Baas *et al.*, 2009; Baker *et al.*, 2017) and in numerical simulations (Garcia, 1994; Felix, 2002; Huang *et al.*, 2007). These experiments show that the addition of a finer fraction makes turbidity currents more efficient, increasing their runout distance, because the flow propagation velocity is maintained for longer due to the reduced sedimentation rate in the presence of lower-settling-velocity particles (Choux & Druitt, 2002; Hodson & Alexander, 2010). The enhanced flow efficiency in the presence of finer grains implies that coarser grains are carried farther out into the basin than in the absence of finer grains. However, initial sediment concentration and particle density play an important role in poly-disperse turbidity currents. Choux & Druitt (2002) found that the lighter particles in two-component flows were very sensitive to initial sediment concentration and were progressively carried farther down the flume with increasing sediment concentration. In contrast, the heavier particles in their experiments were insensitive to initial sediment concentration in controlling runout distance. At elevated concentrations of suspended sediment, the longitudinal sorting of grain size, as controlled by the settling velocity of individual particles, may be altered by the formation of traction carpets on the bed (Sanders, 1965; Hiscott, 1994; Sohn, 1997; Cartigny *et al.*, 2013). For example, in the high-concentration turbidity current deposits of Bell *et al.* (2021), the grain size of the quartz fraction increased downstream, contrasting the model of deposition according to settling velocity. Bell *et al.* (2021) interpreted the downstream increase of grain size as a result of coarse quartz grains being sieved upward in traction carpets while finer

quartz grains at the base were deposited. However, in agreement with Choux & Druitt (2002), Bell *et al.* (2021) reported that high-density grains, on the other hand, were indeed fining downstream, emphasizing the importance of particle density, because heavy particles are possibly affected by sorting mechanisms other than settling.

Particle density. Thus, in bedload sheets forming at higher sediment concentrations, particle density may prevent heavier particles from being sieved upward to the traction carpet surface (Choux & Druitt, 2002; Bell *et al.*, 2021), as normally observed in traction carpets composed of equal-density sediment (Hiscott, 1994; Sohn, 1997). At lower sediment concentrations, that is, below the threshold of traction carpet formation, the effect of particle density was investigated using mixtures of light and heavy particles of similar grain size. If the sediment concentration is kept constant, but the density of a fraction of the particles is increased, then the resulting higher bulk density of the flow leads to an enhanced propagation velocity (Choux & Druitt, 2002; Hodson & Alexander, 2010). However, the runout of the flow (i.e. its efficiency) depends on the time for which the propagation velocity is maintained. The presence of particles with lower settling velocities leads to a reduced sedimentation rate for the entire flow and, thus, by maintaining the propagation velocity for longer, flows with lower settling-velocity particles transport farther into the basin (Choux & Druitt, 2002; Hodson & Alexander, 2010). Choux & Druitt (2002) and Hodson & Alexander (2010) focused on density-segregation processes in two dimensions. Pyles *et al.* (2013), on the other hand, experimentally investigated the effect of particle density in

turbidity currents on the distribution of grain properties in submarine lobes (see also Stammer, 2014). They found that high-density particles are deposited predominantly in the axis of the lobe, and that particle density decreased longitudinally and laterally to the lobe fringes. Hodson & Alexander (2010) argued that carbonate turbidity currents, which are (partly) composed of skeletal components, contain grains with lower density due to intraparticle porosity as typical for bioclasts, giving the examples of crinoids and larger benthic foraminifera. Although Hodson & Alexander (2010) are correct in stating that certain carbonate skeletons, in particular intact foraminifera tests and crinoid ossicles, have a much lower particle density, this statement cannot be taken as generally valid for skeletal grains (see extensive compilation of published carbonate densities in De Kruijf *et al.*, 2021). Nevertheless, a wider distribution of densities is expected for carbonate sands composed of assemblages of skeletal components in comparison to turbidity currents of quartz composition. Yet, also siliciclastic and mixed carbonate–siliciclastic currents may transport a wide range of densities, as a result of multi-mineral composition or due to the presence of porous bioclastic grains such as larger benthic foraminifera (e.g. Ash-Mor *et al.*, 2022a, although the mechanisms initiating gravity flows remain a point of discussion: Reijmer, 2022; Ash-Mor *et al.*, 2022b).

Particle shape. Particle shape determines in large part the fluid drag on settling grains of a given size (Pettyjohn & Christiansen, 1948; Komar & Reimers, 1978). Although there is no universal shape parameter (Blott & Pye, 2008), there is consensus that the effect of shape operates at three different orders of scale: form, roundness and surface texture (Barrett, 1980). *Surface texture* deals with the roughness and irregularity of the particle surface, and is deemed to be of minor importance (Williams, 1966), although this is yet to be evaluated for carbonate grains. *Roundness* concerns the angularity of the corners, and *form* describes the spatial distribution of the particle. On the assumption that siliciclastic grains are largely spheroidal (a premise which may be less unambiguous than generally assumed, see, for example, Fig. 18C), Pyles *et al.* (2013) undertook experiments to examine the influence of particle roundness on the sorting of sediment of the same size and density in turbidite lobes. They found that particle roundness is highest in the axial zone and decreases distally and laterally to the lobe fringes. Pyles *et al.* (2013) attributed the preferential deposition of angular

grains in distal environments to the additional fluid drag generated around particles with sharp corners. A broader approach to the evaluation of particle-shape effects was adopted by Pantopoulos *et al.* (2022), who studied the longitudinal distribution of eleven shape parameters in several turbidite lobe experiments. More than ten thousand particles were analysed from glass-slide samples using two-dimensional particle cross-sections. Pantopoulos *et al.* (2022) stress that shape fractionation in turbidites has potential to be used as a tool for the discrimination of depositional environments in submarine fans. However, many of the two-dimensional shape parameters are not mutually independent of one another (Flemming, 1965; Barrett, 1980). Moreover, two-dimensional shape descriptors cannot fully quantify the shape of three-dimensional particles (e.g. Su & Yan, 2019; Beemer *et al.*, 2022), in particular for calciturbidite deposits wherein grain orientation by hydraulic sorting is important. In the case of skeletal carbonates, the first-order shape descriptor *form* is likely to be the most meaningful shape parameter, although roundness-related parameters can explain additional retardation of the settling velocity.

The shape of the carbonate grains from the calciturbidites produced in the present experiments are analysed, for the first time, in three dimensions. Despite slight distal-fining, the carbonate turbidity currents here revealed measurable shape sorting effects (Figs 16 and 17). The concept of shape sorting in calciturbidites, as a result of differential shape-dependent settling velocities, is shown in Fig. 20. This conceptual model applies to carbonate turbidity currents transporting sediment particles in a narrow grain-size range. Typical skeletal components corresponding to the different Zingg-shape classes are given in Table 4.

Hydraulic sorting versus grain-size (geometric) sorting

Sorting, in a sedimentological sense, is a measure of the mixture of sediment properties. Hydraulic sorting thus describes the extent to which particles have been segregated according to hydraulic equivalence, which for turbidites can be interpreted according to their settling velocity (Bornhold & Pilkey, 1971; van Tassell, 1981; Sadler, 1982; Komar, 1985). Therefore, in a deposit that is *hydraulically well-sorted*, grains with similar settling velocity occur together. In the same way, grain-size sorting expresses the degree to which particles with the same geometry are present in a

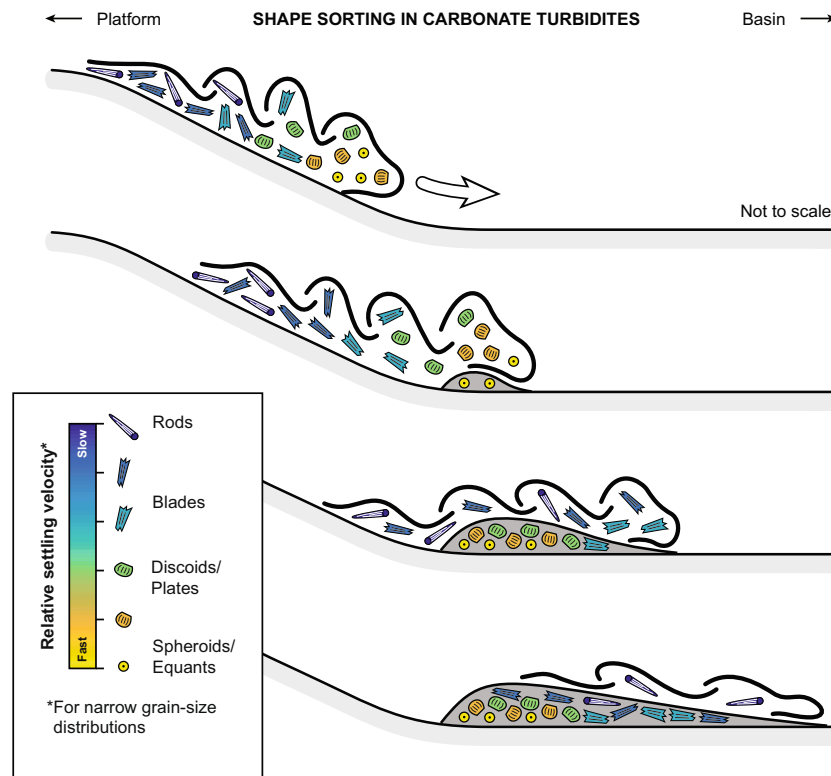


Fig. 20. Shape sorting in carbonate turbidity currents. Interpretation of the particle-shape fractionation mechanism due to differential settling velocities. Grains with the highest settling velocities are preferentially deposited in proximal settings of the turbidite, whereas lower settling-velocity grains reach farther into the basin. The combination of grain size, density and particle shape controls settling velocity. For narrow ranges of grain-size and density, the effect of shape sorting was observed. Shape sorting becomes increasingly significant for larger grain sizes.

sediment sample. Quantification of sorting may be useful to providing insights into depositional processes (Inman, 1949; Folk & Ward, 1957; Plumley *et al.*, 1962). Grain-size sorting is associated with primary porosity, which is of key interest in the industry exploring for subsurface fluids (Porten *et al.*, 2016; Bell *et al.*, 2018).

Because settling velocity depends on the size, density and shape of sediment grains, for a sample composed of spherical particles and in the absence of variation in density, there is no difference between hydraulic sorting and grain-size sorting. In a siliciclastic sediment sample composed of near-spherical quartz grains, hydraulic sorting is identical to grain-size sorting. This concept of grain-size sorting is deeply ingrained in siliciclastic sedimentology (Steidtmann, 1982). However, in the case of sediment with variations in density and/or shape, such as skeletal carbonates, and potentially sediment in numerous siliciclastic environments, this simplified model does not hold.

A turbidite sediment sample represents a settling-velocity distribution of the particles deposited by a turbidity current over a given distance (longitudinal sample) or period of time (vertical sample). The hydraulic distribution of the turbidite sediment sample thus reflects the ‘flow history’ of the turbidity current. This flow history may be taken as a property of the flow associated with that sample. For an ideal sediment population composed of perfectly spherical particles, there is but a single solution of the settling velocity for a given grain size. Assuming a linear approximation of the relationship between settling velocity and lognormal grain size (see Fig. 18), the resulting grain-size sorting of the sample constitutes the projection of the flow history onto the settling velocity curve (Fig. 21A). If the distribution of the flow history is Gaussian, then also the grain-size distribution of the sample is normal-distributed.

When the same turbidity current, characterized by an identical flow history, would have operated

in an environment with irregular skeletal and non-skeletal carbonate grains instead of spheroidal siliciclastic particles, the effect of shape distribution must be incorporated into the modelled prediction of grain-size sorting. Instead of just a single value of grain size for each settling velocity, for carbonate grains there exists a range of grain sizes for each value of the settling velocity. The probabilities of such shape distribution are multiplied with the distribution of the flow history to obtain the grain-size distribution of the sample, i.e. its geometric sorting. For carbonate sediments with a broad range of forms, the resulting grain-size distribution is asymmetrical, skewed towards coarser grain sizes and broader than for spherical sediment (Fig. 21B). The implications of shape distribution are such that, compared to spheroidal siliciclastics, carbonate samples are expected to be more poorly sorted geometrically.

A corollary of this poorer sorting is that carbonate grain accumulations also yield lower primary porosities. Deposits composed of irregular particles differ in packing, i.e. the spatial organization of grains (Von Seckendorff & Hinrichsen, 2021), in comparison with a spherical sediment. Packing influences a sample's porosity (space between particles in a deposit) and permeability (flow rate of fluid passing through that deposit). In addition to packing, also particle arrangement, such as preferred grain orientation during deposition, influences porosity and permeability (Graton & Fraser, 1935). Motivated by a need to evaluate subsurface fluid reserves, these concepts are well-established in sedimentology, especially for isotropic sediment grains like the spherical siliciclastic model, and increasingly also for irregular grains (e.g. Guo *et al.*, 2019). Vinopal & Coogan (1978) investigated the packing of skeletal carbonates in physical experiments using discs and cylinders as well as natural sands. They found that large variations may occur, for example, the packing of perfect spheres, like ooids, leads to a porosity of 43%, while discs and rods yield pore space volumes of 35% and 46%, respectively. Recent studies have used numerical simulations to reconstruct porosity and permeability in deposits composed of more complicated shape mixtures (e.g. Guises *et al.*, 2009). Packing and permeability in skeletal carbonates may lead to anisotropic flow in the pore network, chiefly in the early diagenetic phase (De Boever *et al.*, 2012; Hosa & Wood, 2017). Packing textures and composition also influence geomechanical properties of bioclastic sediments (Shahnazari & Rezvani, 2013; Beemer *et al.*, 2019; Xiao *et al.*, 2019). These properties may influence

fracture patterns associated with secondary porosity (Rusticelli *et al.*, 2016; Miranda *et al.*, 2018; Zambrano *et al.*, 2021). Additional study in this field of research is required to enhance the understanding of porosity and permeability predictions in skeletal carbonates.

Carbonate versus siliciclastic turbidites

Carbonate turbidites may display vertical sequences that are different than observed in siliciclastic turbidites (Meischner, 1964; Eberli, 1991), although Bouma-style beds also occur in carbonates (e.g. Colacicchi & Monace, 1994; Le Goff *et al.*, 2015). These differences are due to contrasting slope and sediment properties between siliciclastic and carbonate slope systems, including irregular carbonate grain shapes, organic binding between grains and early cementation that allow for carbonate slopes with steeper gradients, yet potentially rich in high-cohesive fines (Kenter & Schlager, 1989; Kenter, 1990; Grammer *et al.*, 1993, 1999; Adams & Kenter, 2014; Reolid *et al.*, 2017). In contrast to siliciclastic turbidites, which are introduced from a point-source outside the sedimentary system, carbonates originate within the depositional system (Maiklem, 1968; James, 1997). As a result, margin-parallel carbonate factories may develop laterally-extensive sediment aprons containing channels, lobes and sheets (Colacicchi & Baldanza, 1986; Mullins & Cook, 1986; Playton *et al.*, 2010). However, channel-levée systems and fans, as characteristic for siliciclastic shelf slopes, also occur in carbonate settings (Mulder *et al.*, 2018; Recouvreur *et al.*, 2021), although they seem to be the exception (Mulder *et al.*, 2014). The nature of carbonate grains is in large part determined by the carbonate factory (Schlager, 2000, 2003; Reijmer, 2021). However, sea-level variations need to be considered; for example, the dominance of skeletal components during glacial sea-level lowstands, and non-skeletal abundance during highstands, as demonstrated in the Pleistocene slope deposits of the Bahamas (Haak & Schlager, 1989; Reijmer *et al.*, 1992, 2015). Further discussion of contrasting carbonate and siliciclastic slopes is beyond the scope of this contribution; a review was presented by Adams & Kenter (2014).

From a process perspective, the hydrodynamic properties of carbonate grains control the vertical and longitudinal sorting of calciturbidites in platform-to-basin trajectories (Counts *et al.*, 2021; Le Goff *et al.*, 2021). Detailed outcrop studies focused on the distribution of skeletal and non-

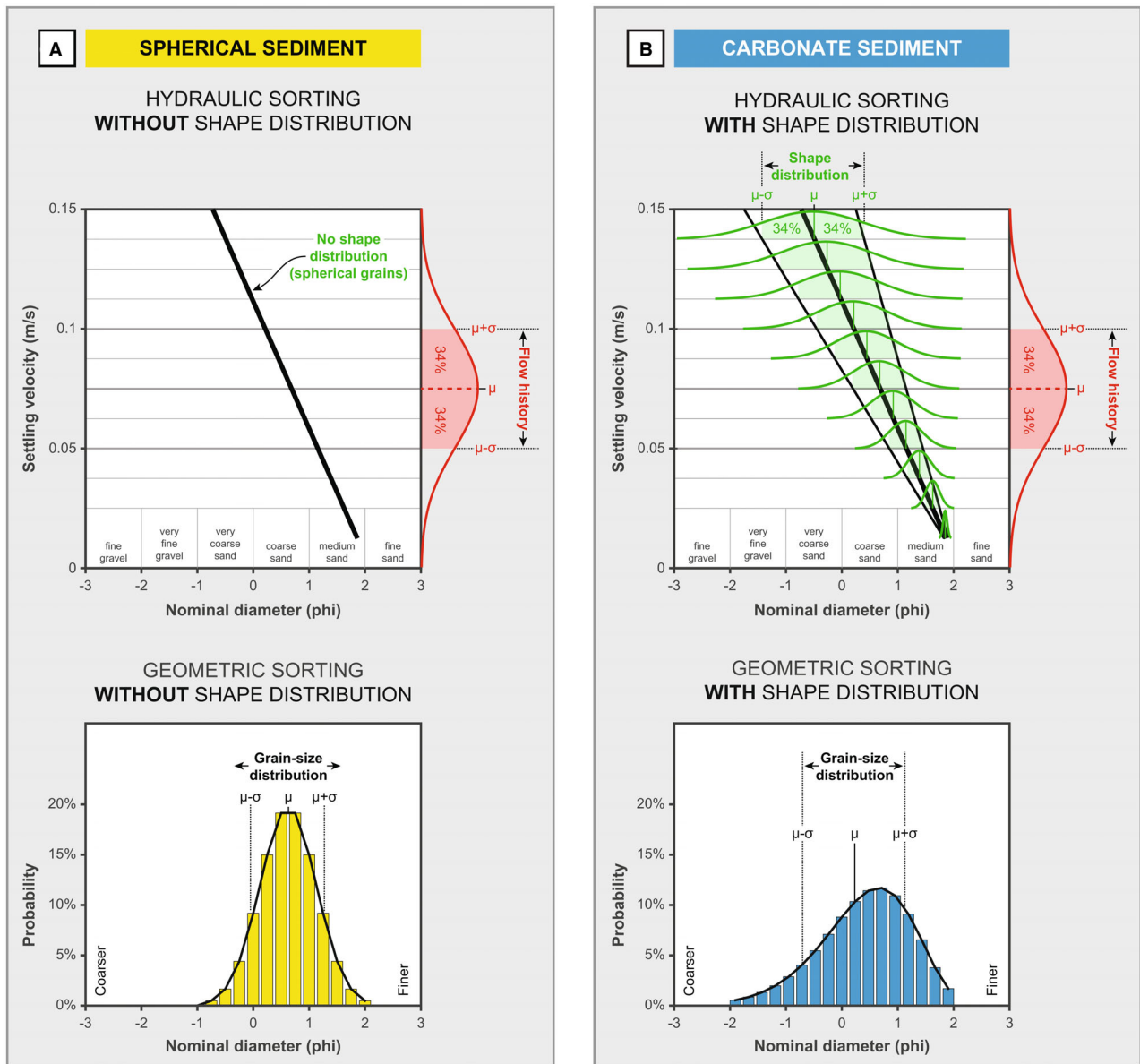


Fig. 21. Influence of shape distribution on geometric sorting and porosity. Hydraulic sorting is the distribution of particle settling velocity within a sediment sample, which is associated with the flow history at the point of deposition. Grain-size distribution (i.e. geometric sorting) is calculated by projecting the flow history onto the linear relationship between settling velocity and grain size (ϕ) as approximated for the Smith & Cheung (2003) carbonate dataset (Fig. 18). One sediment population (yellow) consists uniquely of spherical particles that have no shape distribution. A symmetrical flow history results in a narrow, sharp, symmetrical grain-size distribution in the sample. The carbonate population (blue) is characterized by a shape distribution similar to the carbonate dataset of Smith & Cheung (2003). The same flow history yields a broader, asymmetrical grain-size distribution in the carbonate sample. The carbonate sample contains a larger proportion of coarser sediment than the spherical sample. The carbonate sample is geometrically more poorly sorted than the spherical sample, and thus associated with lower porosity.

skeletal grains in calciturbidites (e.g. Reijmer, 1991; Reijmer & Everaars, 1991, Reijmer *et al.*, 1991, 1994; Herbig & Mamet, 1994). New insights into sediment-gravity flow dynamics,

which are classically developed for siliciclastic sediments, are increasingly applied to the study of ancient carbonate slope deposits (e.g. Kvale *et al.*, 2020). Yet, much understanding is still

obtained from observations in modern carbonate slope-to-basin environments. For example, as intuitively expected, the abundance of neritic sand in carbonate turbidites decreases with

distance from the platform margin (for example, Glorieuses Archipelago, Indian Ocean: Jorry *et al.*, 2020). Likewise, calciturbidites in the Bahamas become thinner and finer-grained with

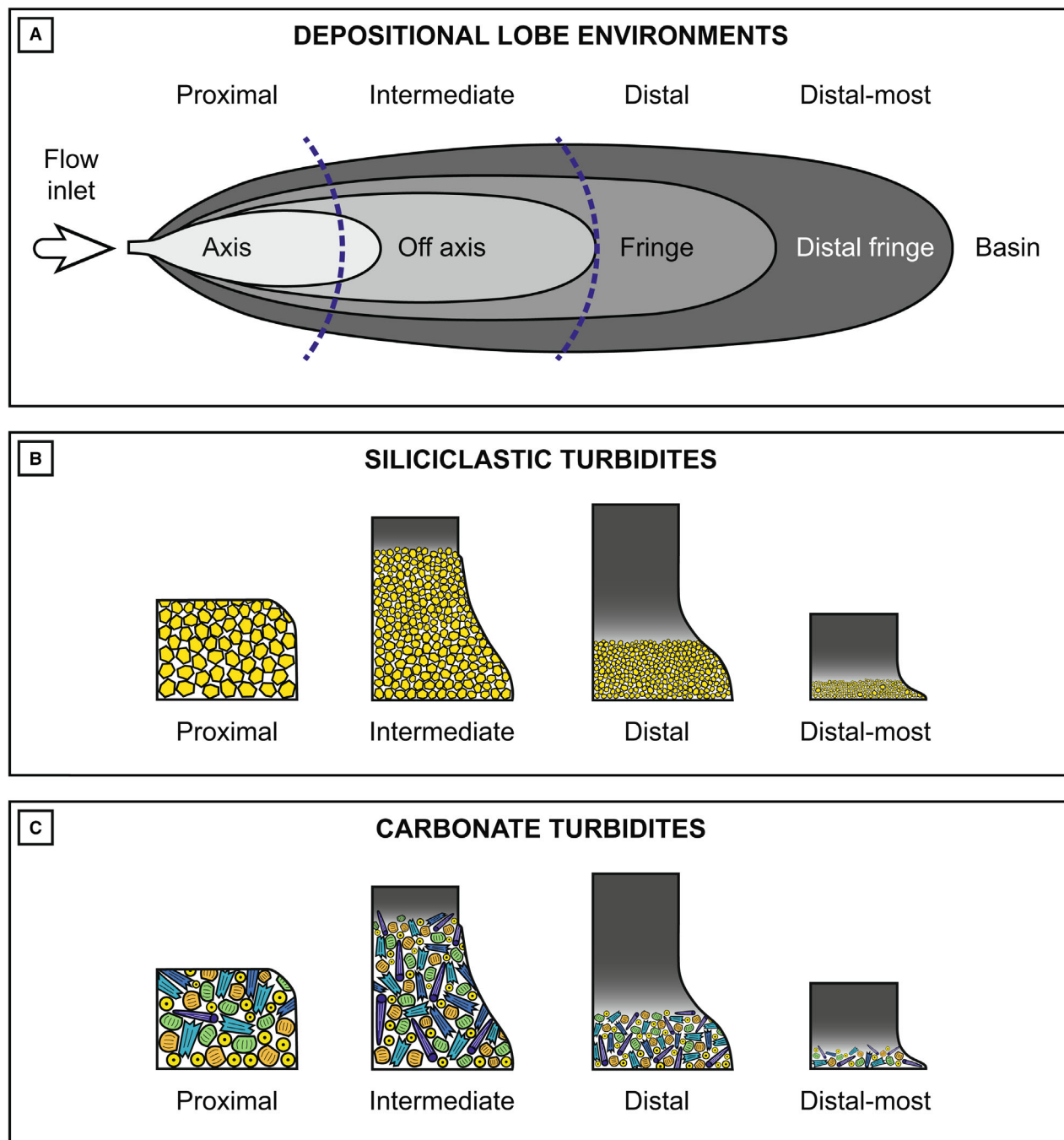


Fig. 22. Carbonate versus siliciclastic turbidites. (A) Schematic plan view of depositional environments on a submarine lobe. Conceptual vertical cross-sections of a (B) siliciclastic turbidite and (C) carbonate turbidite in different subenvironments. Siliciclastic turbidites are fining-upward and fining distally. Distal turbidites become progressively more muddy (darker shades). In the carbonate turbidite, grain types of the same composition are fining-upward and fining distally. However, particles of hydraulic equivalence but with different composition and different grain sizes are deposited together. Bed grading inspired from Bosellini *et al.* (1989).

distance, and more turbidites begin with the horizontal stratification of the Bouma B unit instead of Bouma A (Bornhold & Pilkey, 1971). Compositional variation in calciturbidites revealed a distal decrease in the abundance of *Halimeda* green algae, ooids and pellets, whereas the relative content of planktonic foraminifera and pteropods increased (Bornhold & Pilkey, 1971; Van Tassell, 1981; Andresen *et al.*, 2003). In addition, with distance into the basin high-magnesium calcite may gradually be replaced with low-magnesium calcite, likely representing the influence of particle density (Bornhold & Pilkey, 1971; Le Goff *et al.*, 2021). In the Bahamas, besides grainy turbidites, Bornhold & Pilkey (1971) also reported finer calciturbidites, almost exclusively composed of planktonic foraminifera and pteropods, interpreted to be sourced from farther down the slope rather than the upper slopes and banks.

Longitudinal variation in the composition of calciturbidites, as observed in numerous studies (e.g. Bornhold & Pilkey, 1971; Van Tassell, 1981; Colacicchi & Baldanza, 1986; Brunner & Ledbetter, 1987; Herbig & Mamet, 1994; Bábek & Kalvoda, 2001; Andresen *et al.*, 2003; Maurer *et al.*, 2003; Maurer & Schlager, 2003; Jorry *et al.*, 2020; Counts *et al.*, 2021; Le Goff *et al.*, 2021), is ultimately controlled by the hydrodynamic properties of the transported carbonate grains. This perspective on calciturbidites has received less attention, yet is key to a process-based approach of carbonate slopes. Particle properties, including size, density and shape, determine the fractionation of carbonate grains in the depositional system through differential hydrodynamic behaviour, especially by divergent settling velocities. Also of importance are input constraints to the slope and basin, which are set by variation in facies distribution on the platform (for example, mud-dominated facies versus sand-dominated facies) combined with the distribution of islands, shoals and reefs at the platform margin, as well as the overall morphology of the continental slope (Puga-Bernabéu *et al.*, 2011, 2013). Quantification of these effects is crucial to enhance depositional models, because differences between siliciclastic turbidites and carbonate turbidites is in large part driven by these hydrodynamic contrasts. An important implication hereof is the difference in packing and sorting between siliciclastic and carbonate turbidites, which influence the porosity and permeability distribution in deposits (Fig. 21).

Conceptual cross-sections of siliciclastic and carbonate turbidites in the different submarine

lobe environments are shown in Fig. 22. Particles with hydraulic equivalence are deposited together. The effect of waning flow conditions is expressed by the vertical gradient in particle settling velocity, which is reflected as size-grading in siliciclastic turbidites. In contrast, grains in carbonate turbidites have different shapes, which affect particle settling velocities. Grains of different composition and with different size and shape are therefore deposited together. Yet, particles of the same composition are fining-upward. Grain shapes with higher relative settling velocities (for example, spheres) reach less far into the basin than particle shapes with lower settling velocities (for example, rods). These trends in the composition of calciturbidites provide additional tools for palaeoenvironmental reconstructions and subsurface reservoir modelling.

CONCLUSIONS

Settling velocity is a key parameter in determining the distribution of sediment particles in turbidites, decreasing longitudinally in submarine lobes as well as upward in the deposits of waning turbidity currents. In carbonate depositional systems, in addition to grain size and particle density, the irregular shape of skeletal sediments exerts a significant control on the distribution of sand grains in calciturbidites. The experiments in this study investigated the extent to which the shape of carbonate particles controls a sorting mechanism through differential settling velocities. Three types of experiments were conducted:

1 Free settling of single grains: The influence of particle shape on the settling velocity of individual grains is enhanced as grain size increases. As grains deviate from spheroidal to platy, bladed and elongated forms, for which the Corey Shape Factor is an adequate indicator, the retardation effect of particle shape on the settling velocity is enlarged. The extreme forms with low Corey Shape Factors, typically present in skeletal carbonates, are largely responsible for the wider distribution of settling velocity in carbonates in comparison to siliciclastics, which are typically devoid of extremely non-spheroidal grains.

2 Bulk settling of sediment suspensions: The settling of grains in suspensions is affected by the presence of other particles, which leads to lower settling velocities of individual grains and

the shape-dependent sorting mechanism to be partially obstructed with increasing sediment concentration. In the suspension-cloud settling experiments conducted here, particle shape segregation was strongest at the base and top of the suspension, because fast particles outran the front and slower grains were left behind in the tail. Grains in the body were partly hampered to fall according to their settling velocity. In line with the observations in the single-grain experiments, shape sorting was enhanced as grain size increased.

3 Settling in turbidity currents: Turbidity currents sort particles according to their settling velocity (hydraulic sorting), which for individual grains depends on particle size, density and shape. Previous experiments established the longitudinal sorting of grain size and particle density in turbidites, although basal layers in high-concentration flows (traction carpets) may impede sediment sorting according to settling velocity. The turbidity-current experiments in this study demonstrated that the influence of sorting according to particle shape affects carbonate turbidites, in particular for coarser grain sizes.

Sediment particles in turbidites are hydraulically sorted, i.e. according to hydraulic equivalence in terms of settling velocity. In case of particles with constant density and shape, only grain size controls variations in settling velocity. Grain-size sorting, or geometric sorting, is then identical to hydraulic sorting. If particle shape plays a significant role in determining settling velocity, turbidite samples that are hydraulically well-sorted may be poorly sorted in terms of grain size. This deviation between hydraulic and geometric sorting may result in differences in primary porosity between carbonate and siliciclastic turbidites.

Existing turbidite models are biased towards siliciclastic systems; however there is a growing interest in gravity flows in carbonate environments. Siliciclastic and carbonate slope systems are different, which may have marked effects on gravity-flow triggers and hydrodynamics, and resulting bed styles and architectures. The possibility of steeper slopes, numerous sediment point sources, *in-situ* carbonate production, composition-controlled variations in particle density, organic binding between grains and early cementation should warn against the imprudent application of siliciclastic concepts in the study of carbonate turbidites. This study demonstrated that grain shape must be incorporated into hydrodynamic models of carbonate turbidity currents.

ACKNOWLEDGEMENTS

We are grateful for the financial support received from ARAMCO to JR and AS (CIPR2319 – CRPO6510864832), and additional support by the College of Petroleum Engineering and Geosciences at KFUPM to AS, GG and JR. Discussions with the Geology Technology team at ARAMCO-EXPEC Advanced Research Center provided useful insights and directions. We thank Prof. Cheung for sharing the Smith & Cheung (2003) dataset with us. Janneke van Ginkel is thanked for assistance with the suspension-cloud experiments. Gabriel Yong helped with preliminary experiments with unstoppable enthusiasm. We are indebted to Dr Abdulaziz Al-Kaabi, Dean of the College of Petroleum Engineering and Geosciences at KFUPM, for his continuous sharing of insights into industry needs. Comments and suggestions by Rafael Manica and three anonymous reviewers, and editors Fabrizio Felletti and Jaco Baas, and Elaine Richardson were invaluable in improving the quality of the manuscript.

DATA AVAILABILITY STATEMENT

The data that support the findings of this study are included as [Supplementary Materials](#). The MATLAB scripts used for visualization of the results are available from the corresponding author upon request.

REFERENCES

- Adams, E.W. and Kenter, J.A.M. (2014) So different, yet so similar: comparing and contrasting siliciclastic and carbonate slopes. In: *Deposits, Architecture, and Controls of Carbonate Margin, Slope, and Basinal Settings* (Eds Verwer, K., Playton, T.E. and Harris, P.M.), *SEPM Special Publication*, **105**, 14–25. Special Publication of the Society of Economic Palaeontologists and Mineralogists, Tulsa.
- Alcerreca, J.C., Silva, R. and Mendoza, E. (2013) Simple settling velocity formula for calcareous sand. *J. Hydraul. Res.*, **51**, 215–219.
- Andresen, N., Reijmer, J.J.G. and Droxler, A.W. (2003) Timing and distribution of calciturbidites around a deeply submerged carbonate platform in a seismically active setting (Pedro Bank, Northern Nicaragua Rise, Caribbean Sea). *Int. J. Earth Sci. Geologische Rundschau*, **92**, 573–592.
- Ash-Mor, A., Almogi-Labin, A., Bouchet, V.M.P., Seuront, L., Guy-Haim, T., Ben-Avraham, Z. and Bookman, R. (2022a) Going with the flow: experimental simulation of sediment transport from a foraminifera perspective. *Sedimentology*, **69**, 1231–1251.
- Ash-Mor, A., Almogi-Labin, A., Bouchet, V.M.P., Seuront, L., Guy-Haim, T., Ben-Avraham, Z. and Bookman, R.

- (2022b) Reply to the Comment by John J.G. Reijmer on 'Going with the flow: Experimental simulation of sediment transport from a foraminifera perspective' by Ash-Mor et al. (2022), *Sedimentology*, 69, 1231–1251. *Sedimentology*, 70, 598–601.
- Austin, J.A., Jr., Schlager, W. and Palmer, A.A. (1986) Leg 101. Proceedings initial reports (Pt. A). Ocean Drilling Program, College Station, TX.
- Baas, J.H., Best, J.L., Peakall, J. and Wang, M. (2009) A phase diagram for turbulent, transitional, and laminar clay suspension flows. *J. Sediment. Res.*, 79, 162–183.
- Baas, J.H., Best, J.L. and Peakall, J. (2011) Depositional processes, bedform development and hybrid bed formation in rapidly decelerated cohesive (mud–sand) sediment flows. *Sedimentology*, 58, 1953–1987.
- Baas, J.H., Baker, M.L., Buffon, P., Strachan, L.J., Bostock, H.C., Hodgson, D., Eggenhuisen, J.T. and Spychala, Y.T. (2022) Blood, lead and spheres: a hindered settling equation for sedimentologists based on metadata analysis. *Depositional Rec.*, 8, 603–615.
- Baba, J. and Komar, P.D. (1981) Measurements and analysis of settling velocities of natural quartz sand grains. *J. Sediment. Res.*, 51, 631–640.
- Bábek, O. and Kalvoda, J. (2001) Compositional variations and patterns of conodont reworking in Late Devonian and Early Carboniferous calciturbidites (Moravia, Czech Republic). *Facies*, 44, 211–226.
- Bagnold, R.A. (1954) Experiments on a gravity-free dispersion of large solid spheres in a Newtonian fluid under shear. *Proc. R. Soc. London Ser. A Math. Phys. Sci.*, 225, 49–63.
- Baker, M.L., Baas, J.H., Malarkey, J., Jacinto, R.S., Craig, M.J., Kane, I.A. and Barker, S. (2017) The effect of clay type on the properties of cohesive sediment gravity flows and their deposits. *J. Sediment. Res.*, 87, 1176–1195.
- Baldock, T.E., Tomkins, M.R., Nielsen, P. and Hughes, M.G. (2004) Settling velocity of sediments at high concentrations. *Coast. Eng.*, 51, 91–100.
- Barrett, P.J. (1980) The shape of rock particles, a critical review. *Sedimentology*, 27, 291–303.
- Beemer, R.D., Sadekov, A., Lebrec, U., Shaw, J., Bandini-Maeder, A. and Cassidy, M.J. (2019) Impact of biology on particle crushing in offshore calcareous sediments. In: *Geo-Congress 2019: Geotechnical Materials, Modeling, and Testing*, pp. 640–650. American Society of Civil Engineers, Reston, Virginia.
- Beemer, R.D., Li, L., Leonti, A., Shaw, J., Fonseca, J., Valova, I., Iskander, M. and Pilskaln, C.H. (2022) Comparison of 2D optical imaging and 3D microtomography shape measurements of a coastal bioclastic calcareous sand. *J. Imaging*, 8, 72.
- Bell, D., Kane, I.A., Pontén, A.S., Flint, S.S., Hodgson, D.M. and Barrett, B.J. (2018) Spatial variability in depositional reservoir quality of deep-water channel-fill and lobe deposits. *Mar. Petrol. Geol.*, 98, 97–115.
- Bell, D., Soutter, E.L., Cumberpatch, Z.A., Ferguson, R.A., Spychala, Y.T., Kane, I.A. and Eggenhuisen, J.T. (2021) Flow-process controls on grain type distribution in an experimental turbidity current deposit: implications for detrital signal preservation and microplastic distribution in submarine fans. *Depositional Rec.*, 7, 392–415.
- Betzler, C., Eberli, G.P., Alvarez Zarikian, C.A. and the Expedition 359 Scientists. (2017) *Maldives Monsoon and Sea Level. Proceedings of the International Ocean Discovery Program, 359*. International Ocean Discovery Program, College Station, TX.
- Blott, S.J. and Pye, K. (2008) Particle shape: a review and new methods of characterization and classification. *Sedimentology*, 55, 31–63.
- Bornhold, B.D. and Pilkey, O.H. (1971) Bioclastic turbidite sedimentation in Columbus basin, Bahamas. *Geol. Soc. Am. Bull.*, 82, 1341–1354.
- Bosellini, A., Mutti, E. and Ricci-Lucchi, F. (1989) Rocce e successioni sedimentarie. Utet, Torino, 395 p.
- Bouma, A.H. (1962) Sedimentology of some flysch deposits. A graphic approach to facies interpretation. Doctoral Dissertation, published by Elsevier, Amsterdam.
- Braithwaite, C.J.R. (1973) Settling behaviour related to sieve analysis of skeletal sands. *Sedimentology*, 20, 251–262.
- Brunner, C.A. and Ledbetter, M.T. (1987) Sedimentological and micropaleontological detection of turbidite muds in hemipelagic sequences: an example from the late Pleistocene levee of Monterey Fan, central California continental margin. *Mar. Micropaleontol.*, 12, 223–239.
- Bühler, J. and Papantonio, D. (2001) On the motion of suspension thermals and particle swarms. *J. Hydraul. Res.*, 39, 643–653.
- Buls, T., Anderskov, K., Friend, P.L., Thompson, C.E.L. and Stemmerik, L. (2017) Physical behaviour of Cretaceous calcareous nannofossil ooze: insight from flume studies of disaggregated chalk. *Sedimentology*, 64, 478–507.
- Caromel, A.G., Schmidt, D.N., Phillips, J.C. and Rayfield, E.J. (2014) Hydrodynamic constraints on the evolution and ecology of planktic foraminifera. *Mar. Micropaleontol.*, 106, 69–78.
- Cartigny, M.J.B., Eggenhuisen, J.T., Hansen, E.W.M. and Postma, G. (2013) Concentration-dependent flow-stratification in experimental high-density turbidity currents and their relevance to turbidite facies models. *J. Sediment. Res.*, 83, 1046–1064.
- Chen, J., Yao, Z., Jiang, C.B., Wu, Z.Y., Deng, B., Long, Y.N. and Bian, C. (2022) Experiment study of the evolution of coral sand particle clouds in water. *China Ocean Eng.*, 36, 720–733.
- Cheng, N.S. (1997) Effect of concentration on settling velocity of sediment particles. *J. Hydraul. Eng.*, 123, 728–731.
- Choux, C.M. and Druitt, T.H. (2002) Analogue study of particle segregation in pyroclastic density currents, with implications for the emplacement mechanisms of large ignimbrites. *Sedimentology*, 49, 907–928.
- Clift, R., Grace, J.R. and Weber, M.E. (1978) *Bubbles, Drops, and Particles*. Academic Press, New York.
- Colacicchi, R. and Baldanza, A. (1986) Carbonate turbidites in a Mesozoic pelagic basin: Scaglia Formation, Apennines—comparison with siliciclastic depositional models. *Sed. Geol.*, 48, 81–105.
- Colacicchi, R. and Monace, P. (1994) Pure carbonate gravity flow deposits of the Scaglia basin compared with Central Apennine siliciclastics (Marnoso-Arenacea and Laga): analogies and differences. *Memorie di Scienze Geologiche*, 46, 25–31.
- Cook, H.E., Zhemchuzhnikov, V.G., Zempolich, W.G., Zhaimina, V.Y., Buvtyshkin, V.M., Kotova, E.A., Golub, L.Y., Zorin, A.Y., Lehmann, P.J., Alexeiev, D.V. and Giovannelli, A. (2003) Devonian and Carboniferous carbonate platform facies in the Bolshoi Karatau of southern Kazakhstan: Outcrop analogs for coeval carbonate oil and gas fields in the North Caspian Basin. In: *Paleozoic Carbonates of the Commonwealth of Independent States (CIS): Subsurface Reservoirs and Outcrop Analogs* (Eds Zempolich, W.G. and Cook, H.E.),

- SEPM Special Publication*, **74**, 83–122. Special Publication of the Society of Economic Palaeontologists and Mineralogists, Tulsa.
- Cook, H.E., Zhemchuzhnikov, V.G., Zempolich, W.G., Lehmann, P.J., Alexeiev, D.V., Zhaimina, V.Y. and Zorin, A.Y. (2007) Devonian and Carboniferous carbonate platform facies in the Bolshoi Karatau, southern Kazakhstan: outcrop analogs for coeval carbonate oil and gas fields in the North Caspian Basin. In: *Oil and Gas of the Greater Caspian Area* (Eds Yilmaz, P.O. and Isaksen, G.H.), *AAPG Stud. Geol.*, **55**, 159–163. Special Publication of the Society of Economic Palaeontologists and Mineralogists, Tulsa.
- Corey, A.T. (1949) Influence of shape on the fall velocity of sand grains. Doctoral Dissertation, Colorado State University.
- Counts, J.W., Jorjy, S.J., Vazquez-Riveiros, N., Amy, L.A., Dennielou, E. and Jouet, G. (2021) Sedimentology and distribution of late quaternary calciturbidites and calcidebrites in the Mozambique Channel (Southwest Indian Ocean). *Facies*, **67**, 1–23.
- Davies, R. (1968) The experimental study of the differential settling of particles in suspension at high concentrations. *Powder Technol.*, **2**, 43–51.
- De Boever, E., Varloteaux, C., Nader, F.H., Foubert, A., Békri, S., Youssef, S. and Rosenberg, E. (2012) Quantification and prediction of the 3D pore network evolution in carbonate reservoir rocks. *Oil Gas Sci. Technol. Revue d'IFP Energies nouvelles*, **67**, 161–178.
- De Kruijff, M., Sloomman, A., de Boer, R.A. and Reijmer, J.J.G. (2021) On the settling of marine carbonate grains: review and challenges. *Earth-Sci. Rev.*, **217**, 103532.
- Dietrich, W.E. (1982) Settling velocity of natural particles. *Water Resour. Res.*, **18**, 1615–1626.
- Eberli, G.P. (1991) Calcareous turbidites and their relationship to sea-level fluctuations and tectonism. In: *Cycles and Events in Stratigraphy* (Eds Einsele et al.), pp. 340–359. Springer-Verlag, Berlin.
- Eberli, G.P., Swart, P.K., Malone, M.J. (1997) *Proceedings Ocean Drilling Program, Initial Reports Leg 166*, p. 850. Ocean Drilling Program, College Station, TX, USA.
- Enos, P. (1977) Tamabra Limestone of the Poza Rica Trend, Cretaceous, Mexico. *SEPM Special Publications*, **25**, 273–314.
- Felix, M. (2002) Flow structure of turbidity currents. *Sedimentology*, **49**, 397–419.
- Ferguson, R.I. and Church, M. (2004) A simple universal equation for grain settling velocity. *J. Sediment. Res.*, **74**, 933–937.
- Flemming, N.C. (1965) Form and function of sedimentary particles. *J. Sediment. Res.*, **35**, 381–390.
- Folk, R.H. and Robles, R. (1964) Carbonate sands of Isle Perez, Alacran Reef Complex, Yucatan. *J. Geol.*, **72**, 255–292.
- Folk, R.L. and Ward, W.C. (1957) Brazos River bar [Texas]: a study in the significance of grain size parameters. *J. Sediment. Petrol.*, **27**, 3–26.
- Fouda, A.E. and Capes, C.E. (1977) Hydrodynamic particle volume and fluidized bed expansion. *Can. J. Chem. Eng.*, **55**, 386–391.
- Fukushima, Y., Parker, G. and Pantin, H.M. (1985) Prediction of ignitive turbidity currents in Scripps Submarine Canyon. *Mar. Geol.*, **67**, 55–81.
- Gailani, J.Z., Lackey, T.C., King, D.B., Jr., Bryant, D., Kim, S.C. and Shafer, D.J. (2016) Predicting dredging-associated effects to coral reefs in Apra Harbor, Guam-Part 1: sediment exposure modeling. *J. Environ. Manage.*, **168**, 16–26.
- Ganti, V., Lamb, M.P. and McElroy, B. (2014) Quantitative bounds on morphodynamics and implications for reading the sedimentary record. *Nat. Commun.*, **5**, 1–7.
- Garcia, M.H. (1994) Depositional turbidity currents laden with poorly sorted sediment. *J. Hydraul. Eng.*, **120**, 1240–1263.
- Gladstone, C., Phillips, J.C. and Sparks, R.S.J. (1998) Experiments on bidisperse, constant-volume gravity currents: propagation and sediment deposition. *Sedimentology*, **45**, 833–843.
- Goldberg, K., Kuchle, J., Scherer, C., Alvarenga, R., Ene, P.L., Armelenti, G. and De Ros, L.F. (2017) Re-sedimented deposits in the rift section of the Campos Basin. *Mar. Petrol. Geol.*, **80**, 412–431.
- Gong, C., Wang, Y., Hodgson, D.M., Zhu, W., Li, W., Xu, Q. and Li, D. (2014) Origin and anatomy of two different types of mass-transport complexes: a 3D seismic case study from the northern South China Sea margin. *Mar. Petrol. Geol.*, **54**, 198–215.
- Grammer, G.M., Ginsburg, R.N. and Harris, P.M. (1993) Timing of deposition, diagenesis, and failure of steep carbonate slopes in response to a high-amplitude/high-frequency fluctuation in sea level, Tongue of the Ocean, Bahamas. In: *Carbonate Sequence Stratigraphy: Recent Developments and Applications* (Eds Loucks, R.G. and Sarg, J.F.), pp. 107–131. American Association of Petroleum Geologists, Tulsa, OK, USA.
- Grammer, G.M., Crescini, C.M., McNeill, D.F. and Taylor, L.H. (1999) Quantifying rates of syndepositional marine cementation in deeper platform environments – new insight into a fundamental process. *J. Sediment. Res.*, **69**, 202–207.
- Graton, L.C. and Fraser, H.J. (1935) Systematic packing of spheres: with particular relation to porosity and permeability. *J. Geol.*, **43**(8, Part 1), 785–909.
- Griffiths, J.C. (1967) *Scientific Method in Analysis of Sediments*. McGraw-Hill, New York.
- Guises, R., Xiang, J., Latham, J.P. and Munjiza, A. (2009) Granular packing: numerical simulation and the characterisation of the effect of particle shape. *Granular Matter*, **11**, 281–292.
- Guo, P., Stolle, D. and Guo, S.X. (2019) An equivalent spherical particle system to describe characteristics of flow in a dense packing of non-spherical particles. *Transport Porous Media*, **129**, 253–280.
- Haak, A.B. and Schlager, W. (1989) Compositional variations in calciturbidites due to sea-level fluctuations, late Quaternary, Bahamas. *Geologische Rundschau*, **78**, 477–486.
- Heerema, C.J., Talling, P.J., Cartigny, M.J., Paull, C.K., Bailey, L., Simmons, S.M., Parsons, D., Clare, M.A., Gwiazda, R., Lundsten, E., Anderson, K., Maier, K.L., Xu, J.P., Sumner, E.J., Rosenberger, K., Gales, J., McGann, M., Carter, L., Pope, E. and Monterey Coordinated Canyon Experiment Team (2020) What determines the downstream evolution of turbidity currents? *Earth Planet. Sci. Lett.*, **532**, 116023.
- Herbig, H.G. and Mamet, B. (1994) Hydraulic sorting of microbiota in calciturbidites—a Dinantian case study from the Rheinische Schiefergebirge, Germany. *Facies*, **31**, 930–104.
- Hickey, B.M., MacCready, P., Elliott, E. and Kachel, N.B. (2000) Dense saline plumes in Exuma Sound, Bahamas. *J. Geophys. Res. Oceans*, **105**(C5), 11471–11488.
- Hiscott, R.N. (1994) Traction-carpet stratification in turbidites; fact or fiction? *J. Sediment. Res.*, **64**(2a), 204–208.

- Hodson, J.M. and Alexander, J. (2010) The effects of grain-density variation on turbidity currents and some implications for the deposition of carbonate turbidites. *J. Sediment. Res.*, **80**, 515–528.
- Hohenegger, J. (2006) The importance of symbiont-bearing benthic foraminifera for West Pacific carbonate beach environments. *Mar. Micropaleontol.*, **61**, 4–39.
- Hosa, A. and Wood, R. (2017) Quantifying the impact of early calcite cementation on the reservoir quality of carbonate rocks: a 3D process-based model. *Adv. Water Resour.*, **104**, 89–104.
- Huang, H., Imran, J. and Pirmez, C. (2007) Numerical modeling of poorly sorted depositional turbidity currents. *J. Geophys. Res.*, **112**, C01014.
- Hulsey, J.D. (1961) Relations of settling velocity of sand sized spheres. *J. Sediment. Petrol.*, **31**, 101–112.
- Inman, D.L. (1949) Sorting of sediments in the light of fluid mechanics. *J. Sediment. Res.*, **19**, 51–70.
- James, N.P. (1997) The cool-water carbonate depositional realm. In: *Cool and Temperate Water Carbonates*. Special Publication of the Society of Economic Palaeontologists and Mineralogists, Tulsa, 1–20.
- Janson, X., Kerans, C., Loucks, R., Marhx, M.A., Reyes, C. and Murguía, F. (2011) Seismic architecture of a Lower Cretaceous platform-to-slope system, Santa Agueda and Poza Rica fields, Mexico. *AAPG Bull.*, **95**, 105–146.
- Jenny, M., Dušek, J. and Bouchet, G. (2004) Instabilities and transition of a sphere falling or ascending freely in a newtonian fluid. *J. Fluid Mech.*, **508**, 201–239.
- Johnson, D.W. (1939) *The Origin of Submarine Canyons*. Columbia University Press, New York.
- Jorjy, S.J., Jouet, G., Edinger, E.N., Toucanne, S., Counts, J.W., Miramontes, E., Courgeon, S., Riveiros, N.V., Le Roy, P. and Camoin, G.F. (2020) From platform top to adjacent deep sea: new source-to-sink insights into carbonate sediment production and transfer in the SW Indian Ocean (Glorieuses archipelago). *Mar. Geol.*, **423**, 106144.
- Joshi, S., Duffy, G.P. and Brown, C. (2014) Settling velocity and grain shape of maerl biogenic gravel. *J. Sediment. Res.*, **84**, 718–727.
- Karakitsios, V. (2013) Western Greece and Ionian Sea petroleum systems. *AAPG Bull.*, **97**, 1567–1595.
- Kelham, A. (2011) Investigation into the post-mortem transport of benthic foraminifera. Doctoral Dissertation, University of Hull.
- Kench, P.S. and McLean, R.F. (1996) Hydraulic characteristics of bioclastic deposits: new possibilities for environmental interpretation using settling velocity fractions. *Sedimentology*, **43**, 561–570.
- Kenter, J.A.M. (1990) Geometry and declivity of submarine slopes. Doctoral Dissertation, Vrije Universiteit, Faculty of Earth Sciences, Amsterdam, pp. 128.
- Kenter, J.A.M. and Schlager, W. (1989) A comparison of shear strength in calcareous and siliciclastic marine sediments. *Mar. Geol.*, **88**, 145–152.
- Kermack, W.O., McKendrick, A.G. and Ponder, E. (1930) The stability of suspensions: III. The velocities of sedimentation and of cataphoresis of suspensions in a viscous fluid. *Proc. R. Soc. Edinb.*, **49**, 170–197.
- Kneller, B.C. and McCaffrey, W.D. (2003) The interpretation of vertical sequences in turbidite beds: the influence of longitudinal flow structure. *J. Sediment. Res.*, **73**, 706–713.
- Komar, P.D. (1985) The hydraulic interpretation of turbidites from their grain sizes and sedimentary structures. *Sedimentology*, **32**, 395–408.
- Komar, P.D. and Reimers, C.E. (1978) Grain shape effects on settling rates. *J. Geol.*, **86**, 193–209.
- Krumbein, W.C. (1938) Size frequency distributions of sediments and the normal phi curve. *J. Sediment. Res.*, **8**, 84–90.
- Krumbein, W.C. (1941) Measurement and geological significance of shape and roundness of sedimentary particles. *J. Sediment. Res.*, **11**, 64–72.
- Kuenen, P.H. (1937) Experiments in connection with Daly's hypothesis on the formation of submarine canyons. *Leidse Geologische Mededelingen*, **8**, 327–351.
- Kuenen, P.H. and Migliorini, C.I. (1950) Turbidity currents as a cause of graded bedding. *J. Geol.*, **58**, 91–127.
- Kumbhakar, M., Kundu, S. and Ghoshal, K. (2017) Hindered settling velocity in particle-fluid mixture: a theoretical study using the entropy concept. *J. Hydraul. Eng.*, **143**, 06017019.
- Kvale, E.P., Bowie, C.M., Flentrop, C., Mace, C., Parrish, J.M., Price, B., Anderson, S. and DiMichele, W.A. (2020) Facies variability within a mixed carbonate-siliciclastic sea-floor fan (upper Wolfcamp Formation, Permian, Delaware Basin, New Mexico). *AAPG Bull.*, **104**, 525–563.
- Lamb, M.P., McElroy, B., Kopriva, B., Shaw, J. and Mohrig, D. (2010) Linking river-flood dynamics to hyperpycnal-plume deposits: experiments, theory, and geological implications. *Geol. Soc. Am. Bull.*, **122**, 1389–1400.
- Le Goff, J., Cerepi, A., Swennen, R., Loisy, C., Caron, M., Muska, K. and El Desouky, H. (2015) Contribution to the understanding of the Ionian Basin sedimentary evolution along the eastern edge of Apulia during the Late Cretaceous in Albania. *Sed. Geol.*, **317**, 87–101.
- Le Goff, J., Recouvreux, A., Reijmer, J.J.G., Mulder, T., Ducassou, E., Perellò, M.-C., Hanquiez, V., Gillet, H., Cavailhes, T. and Fabregas, N. (2021) Linking carbonate sediment transfer to seafloor morphology: insights from Exuma Valley, The Bahamas. *Sedimentology*, **68**, 609–638.
- Liang, S.C., Hong, T. and Fan, L.S. (1996) Effects of particle arrangements on the drag force of a particle in the intermediate flow regime. *Int. J. Multiphase Flow*, **22**, 285–306.
- Lokier, S.W. and Fiorini, F. (2016) Temporal evolution of a carbonate coastal system, Abu Dhabi, United Arab Emirates. *Mar. Geol.*, **381**, 102–113.
- Loucks, R.G., Kerans, C., Janson, X. and Marhx Rajano, M.A. (2011) Lithofacies analysis and stratigraphic architecture of a deep-water carbonate debris apron: Lower Cretaceous (latest Aptian to latest Albian) Tamabra Formation, Poza Rica Field area, Mexico. In: *Mass-Transport Deposits in Deepwater Settings* (Eds Shipp, R.C., Weimer, P. and Posamentier, H.W.), *SEPM Special Publication*, **96**, 367–389. Special Publication of the Society of Economic Palaeontologists and Mineralogists, Tulsa.
- Lu, Y., Li, W., Wu, S., Cronin, B.T., Lyu, F., Wang, B., Yang, T. and Ma, B. (2018) Morphology, architecture, and evolutionary processes of the Zhongjian Canyon between two carbonate platforms, South China Sea. *Interpretation*, **6**, SO1–SO15.
- Maiklem, W.R. (1968) Some hydraulic properties of bioclastic carbonate grains. *Sedimentology*, **10**, 101–109.
- Marr, J.G., Harff, P.A., Shanmugam, G. and Parker, G. (2001) Experiments on subaqueous sandy gravity flows: the role of clay and water content in flow dynamics and depositional structures. *Geol. Soc. Am. Bull.*, **113**, 1377–1386.
- Masliyah, J.H. (1979) Hindered settling in a multi-species particle system. *Chem. Eng. Sci.*, **34**, 1166–1168.

- Mathai, V., Zhu, X., Sun, C. and Lohse, D. (2018) Flutter to tumble transition of buoyant spheres triggered by rotational inertia changes. *Nat. Commun.*, **9**, 1–7.
- Maurer, F. and Schlager, W. (2003) Lateral variations in sediment composition and bedding in Middle Triassic interplatform basins (Buchenstein Formation, Southern Alps, Italy). *Sedimentology*, **50**, 1–22.
- Maurer, F., Reijmer, J.J.G. and Schlager, W. (2003) Quantification of input and compositional variations of calciturbidites in a Middle Triassic basinal succession (Seceda, Dolomites, Southern Alps). *Int. J. Earth Sci.*, **92**, 593–609.
- Mazzuca, N., Bruni, A. and Joppen, T. (2015) Exploring the potential of deep targets in the South Adriatic Sea: insight from 2D basin modeling of Croatian offshore. *Geologia Croatica*, **68**, 237–246.
- Meischner, K.D. (1964) Allodapische Kalke. Turbidite in riffnahen Sedimentationsbecken. In: *Turbidites* (Eds Bouma, A.H. and Brouwer, A.), Developments in Sedimentology, Vol. 3, pp. 156–191. Elsevier, Amsterdam.
- Middleton, G.V. (1967) Experiments on density and turbidity currents III: Deposition of sediment. *Can. J. Earth Sci.*, **4**, 475–505.
- Mijnlieff, H.F. (2020) Introduction to the geothermal play and reservoir geology of The Netherlands. *Neth. J. Geosci.*, **99**, e2.
- Miranda, T.S., Santos, R.F., Barbosa, J.A., Gomes, I.F., Alencar, M.L., Correia, O.J., Falcão, T.C., Gale, J.F.W. and Neumann, V.H. (2018) Quantifying aperture, spacing and fracture intensity in a carbonate reservoir analogue: Crato Formation, NE Brazil. *Mar. Petrol. Geol.*, **97**, 556–567.
- Moghadaripour, M., Azimi, A.H. and Elyasi, S. (2017) Experimental study of oblique particle clouds in water. *Int. J. Multiphase Flow*, **91**, 101–119.
- Mohr, H., Draper, S., Cheng, L. and White, D.J. (2016) Predicting the rate of scour beneath subsea pipelines in marine sediments under steady flow conditions. *Coast. Eng.*, **110**, 111–126.
- Morgan, K.M. and Kench, P.S. (2016) Reef to Island sediment connections on a Maldivian carbonate platform: using benthic ecology and biosedimentary depositional facies to examine Island-building potential. *Earth Surf. Process. Landf.*, **41**, 1815–1825.
- Mozafari, M., Gutteridge, P., Riva, A., Geel, K., Garland, J. and Dewit, J. (2019) Facies analysis and diagenetic evolution of the Dinantian carbonates in the Dutch subsurface. SCAN Programme (Seismische Campagne Aardwarmte Nederland).
- Mulder, T. and Alexander, J. (2001) The physical character of subaqueous sedimentary density flows and their deposits. *Sedimentology*, **48**, 269–299.
- Mulder, T., Ducassou, E., Gillet, H., Hanquiez, V., Principaud, M., Chabaud, L., Eberli, G.P., Kindler, P., Billeaud, I., Gonthier, E. and Fournier, F. (2014) First discovery of channel-levee complexes in a modern deep-water carbonate slope environment. *J. Sediment. Res.*, **84**, 1139–1146.
- Mulder, T., Gillet, H., Hanquiez, V., Ducassou, E., Fauquembergue, K., Principaud, M., Conesa, G., Le Goff, J., Ragusa, J., Bashah, S. and Bujan, S. (2018) Carbonate slope morphology revealing a giant submarine canyon (Little Bahama Bank, Bahamas). *Geology*, **46**, 31–34.
- Mullins, H.T. and Cook, H.E. (1986) Carbonate apron models: alternatives to the submarine fan model for paleoenvironmental analysis and hydrocarbon exploration. *Sed. Geol.*, **48**, 37–79.
- Murff, J.D. (1987) Pile capacity in calcareous sands: state of the art. *J. Geotech. Eng.*, **113**, 490–507.
- Murray, S.P. (1970) Settling velocities and vertical diffusion of particles in turbulent water. *J. Geophys. Res.*, **75**, 1647–1654.
- Ngan-Tillard, D., Haan, J., Laughton, D., Mulder, A. and Van der Kolff, A.N. (2009) Index test for the degradation potential of carbonate sands during hydraulic transportation. *Eng. Geol.*, **108**, 54–64.
- Nielsen, P. (1993) Turbulence effects on the settling of suspended particles. *J. Sediment. Res.*, **63**, 835–838.
- Normark, W.R. (1970) Growth patterns of deep-sea fans. *AAPG Bull.*, **54**, 2170–2195.
- Pantin, H.M. (1979) Interaction between velocity and effective density in turbidity flow: phase-plane analysis, with criteria for autosuspension. *Mar. Geol.*, **31**, 59–99.
- Pantopoulos, G., Manica, R., McArthur, A.D. and Kuchle, J. (2022) Particle shape trends across experimental cohesive and non-cohesive sediment gravity flow deposits: implications for particle fractionation and discrimination of depositional settings. *Sedimentology*, **69**, 1495–1518.
- Parker, G., Fukushima, Y. and Pantin, H.M. (1986) Self-accelerating turbidity currents. *J. Fluid Mech.*, **171**, 145–181.
- Payros, A. and Pujalte, V. (2008) Calciclastic submarine fans: an integrated overview. *Earth-Sci. Rev.*, **86**, 203–246.
- Pettyjohn, E. and Christiansen, E.B. (1948) Effect of particle shape on free settling rates of isometric particles. *Chem. Eng. Prog.*, **44**, 157–172.
- Pilkey, O.H., Morton, R.W. and Lutemauer, J. (1967) The carbonate fraction of beach and dune sands. *Sedimentology*, **8**, 311–327.
- Pireno, G.E., Cook, C., Yuliong, D. and Lestari, S. (2009) Berai carbonate debris flow as reservoir in the Ruby Field, Sebuku Block, Makassar Straits: a new exploration play in Indonesia. In: *Proceedings Indonesian Petroleum Association 33rd Annual Convention & Exhibition 2009. Indonesian Petroleum Association*, **19**.
- Playton, T.E., Janson, X. and Kerans, C. (2010) Carbonate slopes. In: *Facies Models 4* (Eds James, N.P. and Dalrymple, R.W.), 4th edn, pp. 449–476. Geological Association of Canada, St. John's, Newfoundland.
- Plumley, W.J., Risley, G.A., Graves, R.W., Jr. and Kaley, M.E. (1962) Energy index for limestone interpretation and classification. In: *Classification of Carbonate Rocks – A Symposium* (Ed Ham, W.D.). *AAPG Special Volumes*, **1**, 85–107.
- Porten, K.W., Kane, I.A., Warchol, M.J. and Southern, S.J. (2016) A sedimentological process-based approach to depositional reservoir quality of deep-marine sandstones: an example from the Springar Formation, northwestern Vøring Basin, Norwegian Sea. *J. Sediment. Res.*, **86**, 1269–1286.
- Posamentier, H.W. and Kolla, V. (2003) Seismic geomorphology and stratigraphy of depositional elements in deep-water settings. *J. Sediment. Res.*, **73**, 367–388.
- Puga-Bernabéu, Á., Webster, J.M., Beaman, R.J. and Guilbaud, V. (2011) Morphology and controls on the evolution of a mixed carbonate-siliciclastic submarine canyon system, Great Barrier Reef margin, north-eastern Australia. *Mar. Geol.*, **289**, 100–116.
- Puga-Bernabéu, Á., Webster, J.M., Beaman, R.J. and Guilbaud, V. (2013) Variation in canyon morphology on the Great Barrier Reef margin, north-eastern Australia: The influence of slope and barrier reefs. *Geomorphology*, **191**, 35–50.
- Pyles, D.R., Straub, K.M. and Stammer, J.G. (2013) Spatial variations on the composition of turbidites due to

- hydrodynamic fractionation. *Geophys. Res. Lett.*, **40**, 3919–3923.
- Recouvreur, A., Fabregas, N., Mulder, T., Hanquiez, V., Fauquembergue, K., Tournadour, E., Gillet, H., Borgomano, J., Poli, E., Kucharski, J.B. and Wilk, S.** (2021) Geomorphology of a modern carbonate slope system and associated sedimentary processes: example of the giant Great Abaco Canyon, Bahamas. *Sedimentology*, **68**, 266–293.
- Reijmer, J.J.G.** (1991) Sea level and sedimentation on the flanks of carbonate platforms. Doctoral Dissertation, Vrije Universiteit, Faculty of Earth Sciences, Amsterdam, pp. 162.
- Reijmer, J.J.G.** (2021) Marine carbonate factories: review and update. *Sedimentology*, **68**, 1729–1796.
- Reijmer, J.J.G.** (2022) Comment on ‘Going with the flow: Experimental simulation of sediment transport from a foraminifera perspective’ by Ash-Mor *et al.* (2022), *Sedimentology*, **69**, 1231–1251. *Sedimentology*, **70**, 592–597.
- Reijmer, J.J.G. and Everaars, J.S.L.** (1991) Carbonate platform facies reflected in carbonate basin facies (Triassic, Northern Calcareous Alps, Austria). *Facies*, **25**, 253–278.
- Reijmer, J.J.G., Ten Kate, W.G.H.Z., Sprenger, A. and Schlager, W.** (1991) Calciturbidite composition related to exposure and flooding of a carbonate platform (Triassic, Eastern Alps). *Sedimentology*, **38**, 1059–1074.
- Reijmer, J.J.G., Schlager, W., Bosscher, H., Beets, C.J. and McNeill, D.F.** (1992) Pliocene/Pleistocene platform facies transition recorded in calciturbidites (Exuma Sound, Bahamas). *Sed. Geol.*, **78**, 171–179.
- Reijmer, J.J.G., Sprenger, A., Ten Kate, W.G.H.Z., Schlager, W. and Krystyn, L.** (1994) Periodicities in the composition of Late Triassic calciturbidites (Eastern Alps, Austria). In: *Orbital Forcing and Cyclic Sequences* (Eds De Boer, P.L. and Smith, D.G.), pp. 323–343. International Association of Sedimentologists, Blackwell, London.
- Reijmer, J.J.G., Palmieri, P. and Groen, R.** (2012) Compositional variations in calciturbidites and calcidebrites in response to sea-level fluctuations (Exuma Sound, Bahamas). *Facies*, **58**, 493–507.
- Reijmer, J.J.G., Palmieri, P., Groen, R. and Floquet, M.** (2015) Calciturbidites and calcidebrites: Sea-level variations or tectonic processes? *Sed. Geol.*, **317**, 53–70.
- Reijmer, J.J.G., Ten Veen, J.H., Jaarsma, B. and Boots, R.** (2017) Seismic stratigraphy of Dinantian carbonates in the southern Netherlands and northern Belgium. *Neth. J. Geosci.*, **96**, 353–379.
- Reolid, J., Betzler, C., Eberli, G.P. and Grammer, G.M.** (2017) The importance of microbial binding in neogene-quadernary steep slopes. *J. Sediment. Res.*, **87**, 567–577.
- Riazi, A., Vila-Concejo, A., Salles, T. and Türker, U.** (2020) Improved drag coefficient and settling velocity for carbonate sands. *Sci. Rep.*, **10**, 1–9.
- Richardson, J.F. and Zaki, W.N.** (1954) Sedimentation and fluidisation, part I. *Trans. Inst. Chem. Eng.*, **32**, 35–53.
- Rusticelli, A., Torrieri, S., Tondi, E., Laurita, S., Strauss, C., Agosta, F. and Balsamo, F.** (2016) Fracture characteristics in Cretaceous platform and overlying ramp carbonates: an outcrop study from Maiella Mountain (central Italy). *Mar. Petrol. Geol.*, **76**, 68–87.
- Sadler, P.M.** (1982) Bed-thickness and grain size of turbidites. *Sedimentology*, **29**, 37–51.
- Sanders, J.E.** (1965) Primary sedimentary structures formed by turbidity currents and related resedimentation mechanisms. In: *Primary Sedimentary Structures and Their Hydrodynamic Interpretation* (Ed Middleton, G.V.), *SEPM Special Publication*, **12**, 84–115. Special Publication of the Society of Economic Palaeontologists and Mineralogists, Tulsa.
- Schlager, W.** (2000) Sedimentation rates and growth potential of tropical, cool-water and mud-mound carbonate factories. In: *Carbonate Platform Systems: Components and Interactions* (Eds Insalaco, E., Skelton, P.W. and Palmer, T.J.), *Geological Society Special Publications*, **178**, 217–227. Geological Society, London.
- Schlager, W.** (2003) Benthic carbonate factories of the Phanerozoic. *Int. J. Earth Sci.*, **92**, 445–464.
- Schulz, E.F., Wilde, R.H. and Albertson, M.L.** (1954) Influence of shape on the fall velocity of sedimentary particles. Doctoral Dissertation, Colorado State University.
- Scorer, R.S.** (1997) *Dynamics of Meteorology and Climate*. Praxis Publishing Ltd., Singapore.
- Sequeiros, O.E., Naruse, H., Endo, N., Garcia, M.H. and Parker, G.** (2009) Experimental study on self-accelerating turbidity currents. *J. Geophys. Res.*, **114**, C05025.
- Shahnazari, H. and Rezvani, R.** (2013) Effective parameters for the particle breakage of calcareous sands: an experimental study. *Eng. Geol.*, **159**, 98–105.
- Shen, Y., Feng, Z., Qi, W., Ma, Y. and Liu, H.** (2019) Sedimentary characteristics of coral mud in the South China Sea during the reclamation process. *Geo-Mar. Lett.*, **39**, 417–425.
- Shipboard Scientific Party.** (2001) Leg 194 Preliminary Report. ODP Preliminary Report, 94. http://www-odp.tamu.edu/publications/prelim/194_prel/194PREL.PDF.
- Slootman, A., De Boer, P.L., Cartigny, M.J.B., Samankassou, E. and Moscardiello, A.** (2019) Evolution of a carbonate delta generated by gateway-funnelling of episodic currents. *Sedimentology*, **66**, 1302–1340.
- Slootman, A., De Kruijf, M., Jobe, Z.R., Glatz, G. and Reijmer, J.J.G.** (2023) Shape, volume-to-area ratio, and settling-velocity models for siliciclastic, carbonate, volcanic and plastic particles and their sedimentary implications. In: *Proceedings of the 36th Meeting of Sedimentology*. International Association of Sedimentology, Dubrovnik, Croatia.
- Smith, D.A. and Cheung, K.F.** (2003) Settling characteristics of calcareous sand. *J. Hydraul. Eng.*, **129**, 479–483.
- Sohn, Y.K.** (1997) On traction-carpet sedimentation. *J. Sediment. Res.*, **67**, 502–509.
- Spearman, J. and Manning, A.J.** (2017) On the hindered settling of sand-mud suspensions. *Ocean Dynam.*, **67**, 465–483.
- Spence, G.H. and Tucker, M.E.** (1997) Genesis of limestone megabreccias and their significance in carbonate sequence stratigraphic models: a review. *Sed. Geol.*, **112**, 163–193.
- Spychala, Y.T., Eggenhuisen, J.T., Tilston, M. and Pohl, F.** (2020) The influence of basin setting and turbidity current properties on the dimensions of submarine lobe elements. *Sedimentology*, **67**, 3471–3491.
- Stammer, J.G.** (2014) Hydrodynamic fractionation of minerals and textures in submarine fans: quantitative analysis from outcrop, experimental, and subsurface studies. Doctoral Dissertation, Colorado School of Mines.
- Steidtmann, J.R.** (1982) Size-density sorting of sand-size spheres during deposition from bedload transport and implications concerning hydraulic equivalence. *Sedimentology*, **29**, 877–883.
- Stevenson, C.J., Jackson, C.A.L., Hodgson, D.M., Hubbard, S.M. and Eggenhuisen, J.T.** (2015) Deep-Water Sediment Bypass. *J. Sediment. Res.*, **85**, 1058–1081.

- Su, D.** and **Yan, W.M.** (2019) Prediction of 3D size and shape descriptors of irregular granular particles from projected 2D images. *Acta Geotechnica*, **15**, 1533–1555.
- Swart, P.K., Eberli, G.P., Malone, M.J. and Sarg, J.F.** (Eds) (2000) *Proceedings of the Ocean Drilling Program, Leg 166, Scientific Results*, p. 213. Ocean Drilling Program, College Station, TX.
- Swinchatt, J.P.** (1965) Significance of constituent composition, texture and skeletal breakdown in some recent carbonate sediments. *J. Sediment. Petrol.*, **35**, 71–90.
- Talling, P.J., Amy, L.A. and Wynn, R.B.** (2007) New insight into the evolution of large-volume turbidity currents: comparison of turbidite shape and previous modelling results. *Sedimentology*, **54**, 737–769.
- Tanos, C.A., Kupecz, J., Warren, J.K., Lestari, S. and Baki, A.** (2012) Depositional and diagenetic effects on reservoir properties in carbonate debris deposits: comparison of two debris flows within the Beraí Fm., Makassar Strait, Indonesia. In: *AAPG Search and Discovery Article #50768*. AAPG International Conference & Exhibition, Singapore.
- Thacker, W.C. and Lavelle, J.W.** (1977) Two-phase flow analysis of hindered settling. *Phys. Fluids*, **20**, 1577–1579.
- Tomkins, M.R., Baldock, T.E. and Nielsen, P.** (2005) Hindered settling of sand grains. *Sedimentology*, **52**, 1425–1432.
- Turner, J.S.** (1973) *Buoyancy Effects in Fluids*. Cambridge University Press, Cambridge.
- Uhlmann, M. and Doychev, T.** (2014) Sedimentation of a dilute suspension of rigid spheres at intermediate Galileo numbers: the effect of clustering upon the particle motion. *J. Fluid Mech.*, **752**, 310–348.
- Van Tassell, J.** (1981) Silver abyssal plain carbonate turbidite: flow characteristics. *J. Geol.*, **89**, 317–333.
- Vaz, M.F. and Fortes, M.A.** (1988) Grain size distribution: the lognormal and the gamma distribution functions. *Scripta Metallurgica*, **22**, 35–40.
- Veldhuis, C.H.J. and Biesheuvel, A.** (2007) An experimental study of the regimes of motion of spheres falling or ascending freely in a Newtonian fluid. *Int. J. Multiphase Flow*, **33**, 1074–1087.
- Vinopal, R.J. and Coogan, A.H.** (1978) Effect of particle shape on the packing of carbonate sands and gravels. *J. Sediment. Res.*, **48**, 7–24.
- Von Seckendorff, J. and Hinrichsen, O.** (2021) Review on the structure of random packed-beds. *Can. J. Chem. Eng.*, **99**, S703–S733.
- Wadell, H.** (1932) Volume, shape, and roundness of rock particles. *J. Geol.*, **40**, 443–451.
- Wang, Y., Zhou, L., Wu, Y. and Yang, Q.** (2018) New simple correlation formula for the drag coefficient of calcareous sand particles of highly irregular shape. *Powder Technol.*, **326**, 379–392.
- Wentworth, C.K.** (1922) A scale of grade and class terms for clastic sediments. *J. Geol.*, **30**, 377–392.
- Williams, G.P.** (1966) Particle roundness and surface texture effects on fall velocity. *J. Sediment. Res.*, **36**, 255–259.
- Wilson, P.A. and Roberts, H.H.** (1992) Carbonate-periplatform sedimentation by density flows: a mechanism for rapid off-bank and vertical transport of shallow-water fines. *Geology*, **20**, 713–716.
- Wilson, P.A. and Roberts, H.H.** (1995) Density cascading; off-shelf sediment transport, evidence and implications, Bahama Banks. *J. Sediment. Res.*, **65**(1a), 45–56.
- Xiao, Y., Yuan, Z., Chu, J., Liu, H., Huang, J., Luo, S.N., Wang, S. and Lin, J.** (2019) Particle breakage and energy dissipation of carbonate sands under quasi-static and dynamic compression. *Acta Geotechnica*, **14**, 1741–1755.
- Yordanova, E.K. and Hohenegger, J.** (2007) Studies on settling, traction and entrainment of larger benthic foraminiferal tests: implications for accumulation in shallow marine sediments. *Sedimentology*, **54**, 1273–1306.
- Zambrano, M., Volatili, T., Mancini, L., Pitts, A., Giorgioni, M. and Tondi, E.** (2021) Pore-scale dual-porosity and dual-permeability modeling in an exposed multi-facies porous carbonate reservoir. *Mar. Petrol. Geol.*, **128**, 105004.
- Zingg, T.** (1935) Beitrag zur Schotteranalyse. Doctoral Dissertation, ETH Zurich.

Manuscript received 4 January 2023; revision accepted 26 April 2023

Supporting Information

Additional information may be found in the online version of this article:

Data S1. Experiment conditions and measurement results (spreadsheet).

Table S1. Volume calibration and density determination (spreadsheet).

Video S1. Suspension-cloud experiment with SC-finer.

Video S2. Suspension-cloud experiment with SC-coarser.

Video S3. Turbidity-current experiment with TC-finer.